IEEE Access
Multidisciplinary | Rapid Review | Open Access Journal

Received December 30, 2021, accepted January 11, 2022, date of publication January 14, 2022, date of current version January 21, 2022.

Digital Object Identifier 10.1109/ACCESS.2022.3143166

A Comparative Study of Dual Stator With Novel Dual Rotor Permanent Magnet Flux Switching Generator for Counter Rotating Wind Turbine Applications

WASIQ ULLAH, (Graduate Student Member, IEEE), FAISAL KHAN, (Member, IEEE), AND SHAHID HUSSAIN, (Graduate Student Member, IEEE)

Department of Electrical and Computer Engineering, COMSATS University Islamabad, Abbottabad Campus, Abbottabad 22060, Pakistan

Corresponding author: Wasiq Ullah (wasiqullah014@gmail.com)

ABSTRACT Compared with the single rotor wind turbine, a counter-rotating (CR) wind turbine with two rotor sets leads to twice power density. In this regard, dual stator CR (DSCR) permanent magnet flux switching generator (DSCR-PMFSG) is employed. However, in DSCR-PMFSG both rotor and armature parts are rotating and require slip rings for power transmission. These slip rings associate demerits of constant maintenance, poor speed regulation, increased cost, and additional slip ring losses, whereas DSCR-PMFSG offer lower flux and lesser power density. To overcome the demerits of DSCR-PMFSG as mentioned earlier, this paper proposed a novel dual rotor counter-rotating permanent magnet flux switching generator (DRCR-PMFSG) for wind turbine applications that eliminate the requirements of slip rings and retain brushless operation. The proposed DRCR-PMFSG share one stator connected back-to-back through a flux bridge that provides an alternate flux path between two mechanical ports associated with the inner rotor and outer rotor, contributing to the cumulative output. A detailed comparative analysis of DSCR-PMFSG and DRCR-PMFSG is performed under static characteristics, overload, and wide speed range to generate output power, voltage, current, power density, and efficiency. Quantitative comparative analysis under static analysis evident that proposed DRCR-PMFSG exhibits 33.29% higher flux, suppressed cogging torque and torque ripples up to 53.48% and 67.45%, respectively. Furthermore, a comprehensive quantitative analysis is performed under coupled overload and over-speed capability. Analysis exposes that in comparison with DSCRP-PMFSG, the proposed DRCR-PMFSG improves voltage regulation factor by 55.88%, output current enhanced by 67.9%, raise output voltage to 2.01 times, and power density to 1.72 times while maintaining the efficiency of 90.195% and achieving stable voltage profile with load variation. Finally, a detailed comparative analysis with conventional designs is performed and comprehensive mathematical modelling based on sub-domain model is developed accounting stator slot and rotor pole combinations, magnetic saturation, and winding configuration to validates finite element analysis (FEA) of JMAG Designer v.20.1.

INDEX TERMS Flux switching machines, ferrite permanent magnet, counter rotation, wind turbines, wind power generator, wind power application.

I. INTRODUCTION

Compared with non-renewable energy, wind energy emerged as the most economical and feasible fast-growing renewable energy source for wind power generation, with an installed capacity of 744 GW by the end of 2020 [1]. Wind energy conversion is based on the direct coupling of horizontal/vertical axis wind turbines with the shaft of generators that contributes to the power supplied to local grids, microgrids, or national grid or even energy storage systems in batteries for later uses. This encourages researcher interest in designing wind power generators to improve kinetic energy conversion of wind to electrical energy.

The associate editor coordinating the review of this manuscript and approving it for publication was Xiaodong Lian.

Several solutions emerge for improving wind energy conversion efficiency of wind turbines. One technique for enhancing conversion is to improve wind turbine power coefficient; however, based on wind turbine theory, maximum power coefficient is limited by Bet'z law [2]. Therefore, alternate techniques are preferred to improve wind turbine power coefficient and wind energy conversion efficiency.

From a design perspective, a wide range of permanent magnet (PM) flux switching machines (PMFSMs) are investigated with unique flux nature, i.e., axial flux [3] and transverse flux [4]. In contrast, PMFSM with segmented PM consequent pole configuration is thoroughly investigated [5]–[8]. Besides flux nature and stator PM magnetization, numerous PMFSM is investigated with different rotor position, i.e., inner rotor [9], [10], outer rotor [11], [12], and dual rotor configuration [13], [14] with various stator configuration to achieve maximum power density. Due to better utilization of the available area to achieve higher pole numbers and direct rotor coupling with turbine blades, inner rotor PM flux switching generator (PMFSG) configurations attract researcher interest; however, utilization of the inner area is still poor [15].

To efficiently utilize the available space, dual rotor flux switching generators are introduced that results higher power density [16], [17]. Dual rotor machines have become one of the hot topics in electric machine research area due to independent power transform among two mechanical port and reduced weight and volume. Author in [18] proposes dual rotor structure to improve output torque however, with the improvement in torque, other motor performance such as back-EMF deteriorates and results higher order harmonics content.

The torque density in dual rotor is improved by introducing drum winding machine [14]. Due to drum winding configuration, the developed topology improves flux linkages. Comparative analysis of dual rotor drum winding topology with dual rotor concentrated winding are investigated to show superiority of higher torque by drum winding topology however, stator of the dual rotor with drum topology becomes slightly complex due to different winding toward inner and outer rotor resulting different stator slots shapes as well. Author in [19] proposed dual rotor with toroidal coil connection and modular stator embedded PMs inside upper and lower armature slot modules. This design results sinusoidal back-EMF and flux linkages with reduced cogging torque ripples however, this configuration exhibits leakage flux in the outer shell of stator causing eddy current losses. A new dual rotor with focus on optimization for multi-mode operation is discussed in [20] however, inner rotor occupies PMs and armature winding therefore, associates mechanical constraints and requires slip rings. Thus, to retain brushless operation yokeless dual rotor is investigated in [21] and brushless dual rotor for power allocation is investigated in [22], however, narrow flux barriers may saturate that degrades overall performance.

Despite of dual-rotor topologies, partitioned stator structure had been research interest over the past few decades. Author in [23] introduced hybrid excited partitioned stator occupying armature winding in outer stator and field excitation coils with PMs in inner stator which are sandwich between segmented rotor pieces. This structure shows advantages of achieving flux regulation capability however it shows trade-off with output torque as it is affected by hybridization ratio. Moreover, partitioned stator with different PMs arrangements is investigated in [24], influence with the PM types such as ferrite and NdFeB are studied in [25] and analysis with single and double-layer winding are examined in [26]. It is found that winding arrangement shows slight influence on performance of partitioned stator topologies whereas NdFeB offer excellent results performance in comparison with ferrite PMs. In additional, partitioned stator in [27] harness two distinct synergies phenomena of magnetically geared and switched flux. However, lack flux adjustor which is incorporated in [28] to further improve torque density.

Despite of partitioned stator, authors in [29] introduced segmental rotor permanent magnet flux switching machines with radially magnetized PMs on stator teeth's that results high torque density however, despite of the quasi back-EMF with dominant even-order harmonics, the structure face manufacturing complexity of arc-type PM to maintain constant airgap and difficult cooling mechanism is required for PMs placed at stator teeth. This concept of segmented rotor is extended to Switched Reluctance Machine (SRM) in the form of dual segmented rotor [30] however, despite of manufacturing complexity of rotor segments holder, SRM suffers from low torque and power density. Furthermore, modular stator is investigated in [31] to achieve fault tolerant capability however, in modular stator topology as the PM width increases the reverse flow of flux enlarged resulting degradation of electromagnetic performances especially torque density.

To achieve high torque density, different studies have been conducted with the time over different dual stator topologies. A low pole dual-stator topology is studied in [32], [33] whereas multi-PM MMF harmonic is studied in [34] to achieve high torque and power density. Low pole dual stator topology shows disadvantage of large machine volume due to axially coupling of two rotor and stator whereas dual stator configuration with multi-PM MMF suffers from mechanical constraints and are not feasible for high-speed applications due to segmented discrete rotor pieces. The aforesaid demerits are incorporated in dual stator with fractional slot distributed winding in [35] that results higher torque density however, due to distributed winding configuration, the overhang effect increases, resulting an increase in copper consumption and losses.

Concept of dual stator configuration has been extensively studied to achieve higher power density in counter-rotation generator topologies also. In this regard, a brushless double-fed induction generator (DFIG) for counter-rotating turbines is introduced in [36], DFIG endure high manufacturing cost

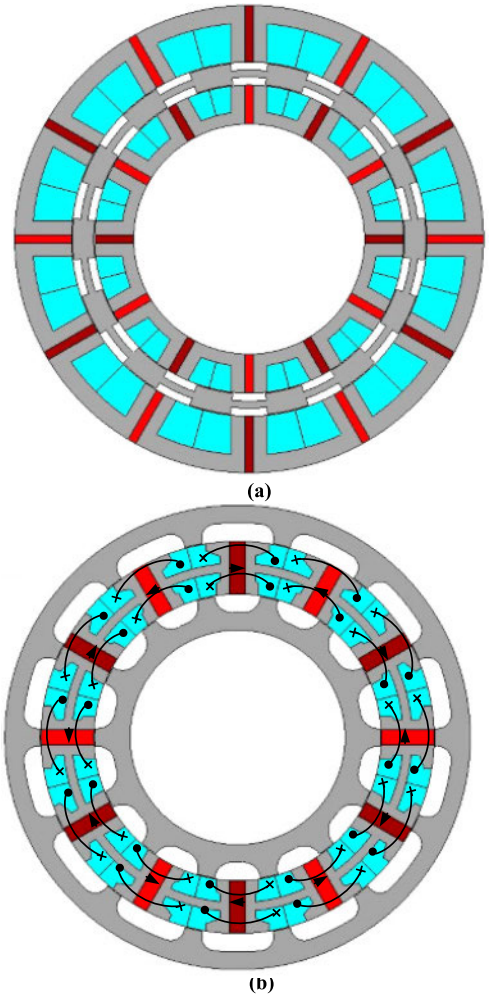

FIGURE 1. Topology of PMFSG (a) Conventional DSCR-PMFSG and (b) Proposed DRCR-PMFSG.

and large dimensions in direct-drive applications [37]. To further improve the power density and overcome the said demerits of DFIG, author's in [38], [39] introduce dual stator counter-rotating PMFSG (DSCR-PMFSG) for wind turbine applications as shown in Figure. 1(a). However, in dual stator configuration, both the rotor and stator rotate in the opposite direction to achieve counter-rotation resulting complexity in the mechanical assembly parts and involving sliding contacts (slip rings and brushes) which are associated with wear and tear therefore, requires constant maintenance. The involvement of the slip ring in a dual stator eliminated brushless operation and made it a brushed-type machine associated with friction losses. Moreover, due to rotation of the active part, i.e., stator housing enclosing PM and armature winding, the impact of the centrifugal force on PMs becomes dominant, and generated heat from the active part that result PM demagnetization.

To overcome the aforesaid demerits of PM demagnetization in DSCR-PMFSG, friction loss in slip ring of DSCR-PMFSG and dual rotor occupying armature winding and PMs in inner rotor, eliminating slip ring requirements to

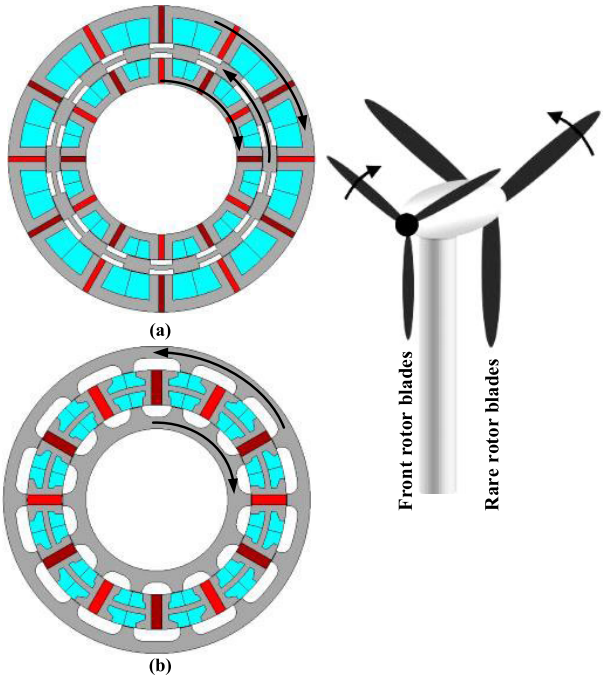

FIGURE 2. Illustration of DDCRWT in DSCR-PMFSG and DRCR-PMFSG.

retain brushless operation in comparison with brushed operation of dual operating mode dual rotor and DSCR-PMFSG, complex assembly and leakage flux issues of partitioned stator, issues of reverse flux flow in modular stator structure, friction losses of DSCR-PMFSG, overhang effect of distributed winding in dual-stator topology and further improvement in torque and power density, this paper proposes a novel dual rotor counter-rotating PMFSG (DRCR-PMFSG) with single tooth non-overlapped concentrated winding for counter-rotating wind power generation as shown in Figure. 1(b). In the proposed DRCR-PMFSG, two sets of rotors rotate in opposite directions to achieve counter-rotation. In contrast, the stationary stator part remains static, eliminating the requirements of the slip ring and retaining brushless operation. Counter rotation in the proposed DRCR-PMFSG is achieved so that the inner rotor rotates clockwise, whereas the outer rotor rotates in an anti-clockwise direction. This counter-rotation not only improves power density but also retains the inherent brushless operation of flux switching.

In counter-rotation, the relative speed between two armatures is larger, resulting in higher power generation at the same stator size, indicating a diminished utilization of active materials. Despite reduced material and high-power density, dual rotor topology exhibits advantages of short flux path resulting lower equivalent iron reluctance. It is important to note that in comparison with DSCR-PMFSG, the proposed DRCR-PMFSG offer advantages of two mechanical ports for independent energy transfer between two mechanical ports, i.e., inner rotor and outer rotor where each port individually act like a separate generator such that one output is taken from the inner armature, 2nd output is taken from the corresponding

outer armature portion, whereas the cumulative response is a summation of both inner and outer mechanical output ports. Therefore, this paper aims to present a detailed investigation of both DSCR-PMFSG and DRCR-PMFSG for wind turbine applications in terms of the static characteristics, overload, and over-speed capability.

The rest of the article is organized as, Section II discusses direct-drive counter-rotating wind turbines. Section III investigated the design concept of DSCR-PMFSG and DRCR-PMFSG. Sub-Domain Model is developed in Section IV, Static analysis is analysed in section V, generating power performance is investigated in section VI. Comparison of conventional and proposed DRCR-PMFSG is evaluated in section VII and finally, some conclusions are drawn in section VIII.

II. DIRECT DRIVE COUNTER ROTATING WIND TURBINES

Numerous techniques for improving the conversion efficiency of wind kinetic energy into electricity have been studied in the last few decades. Among which Direct drives counter-rotating wind turbines (DDCRWT) are the most efficient ones. In this technique, the wind turbine is classified based on rotational direction and spinning rotor. DDCRWT is a type of dual-rotor wind turbine (DRWT) where two sets of rotors are made to rotate in co-rotation or counter-rotation. It is noteworthy that co-rotation is simply the rotation of both front and rare rotors in the same direction. Therefore, the focus will be on counter-rotation in the dual rotor and dual stator configuration.

DDCRWT comprises two sets of rotors blades connected at the front and a rare side rotating in the opposite direction (counter-rotating), as shown in Figure 2. It can be clearly seen that in DDCRWT, the front rotor blades rotate in a clockwise direction, whereas the rare rotor blades rotate in a counter-clockwise direction. It is worth noting that both upstream and downstream are assumed to be uninformed, where both front and rare rotor blades have the same rotational speed.

In the case of DSCR-PMFSG, there are two sets of armatures consisting of circumferential magnetized sandwich PMs between stator cores. For counter-rotation wind power generation, the rotor is connected to rare wind turbine blades, whereas both inner and outer armature set is coupled with the front set of a wind turbine. It is worth noting that in the case of DSCR-PMFSG both rotor and armature parts rotate in opposite directions. Since the armature part in DSCR-PMFSG is not fixed and rotating, slip rings connections must be connected with the phase winding during rotation of inner and outer armature rotation. The connected slip ring is associated with sliding friction losses, and this connection makes the operation of DSCR-PMFSG a brushed operation that requires constant maintenance.

The aforesaid problem is compensated in the proposed DRCR-PMFSG. In the case of DRCR-PMFSG, the front rotor blades are directly coupled to inner rotors to be rotated in clockwise direction, whereas the rare rotor blades are coupled to the outer rotor. To achieve the counter rotating, both the rotor blades are designed to rotate in the counter-clockwise direction. The counter-rotation of the wind turbine can also be achieved in a non-direct drive

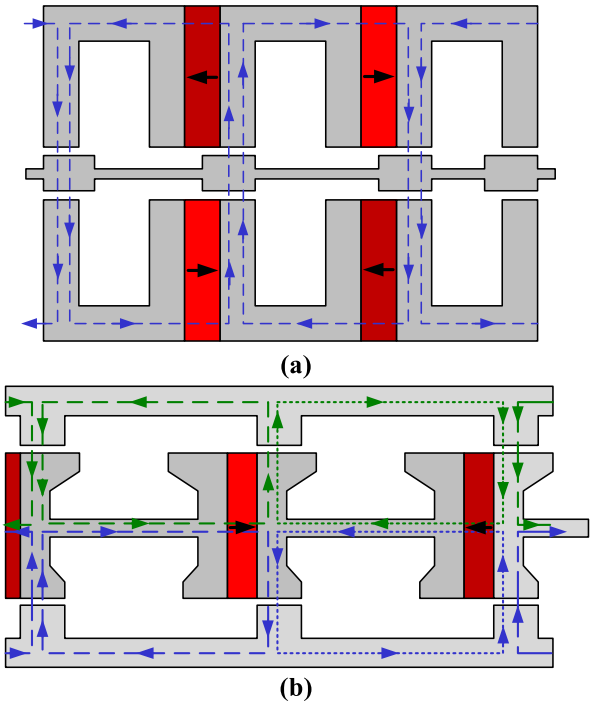

FIGURE 3. Linear illustration of magnetic flux path in (a) conventional DSCR-PMFSG and (b) DRCR-PMFSGs.

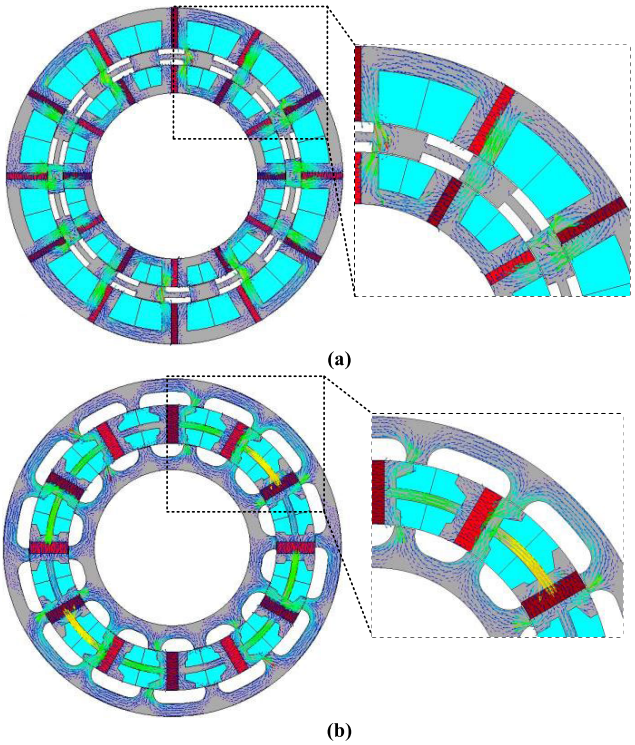

FIGURE 4. FEA based magnetic flux path in (a) conventional DSCR-PMFSG and (b) DRCR-PMFSGs.

system in the proposed DRCR-PMFSG utilizing a co-axial gearbox.

Power density comparison of DRCR-PMFSG with single rotor/wind turbine and direct drive co-rotating wind turbines reveals that DRCR-PMFSG generate higher power density due to two sets of rotors blades which lies in front and rare sides of wind turbines rotating in the opposite direction. The resultant power is generated due to front and rare side wind turbines resulting in double power generation.

III. DESIGN CONCEPT OF DSCR-PMFSG AND DRCR-PMFSG

Similar to conventional PMFSG, high power density and reliability features are retained in conventional DSCR-PMFSG and DRCR-PMFSG where rotors are robustly made of stacked silicon steel sheets and all the excitation sources, i.e., armature winding, and PMs are housed inside the stator. DSCR-PMFSG comprises two armatures, i.e., inner armature and outer armature, whereas one rotor in between both armatures. Each armature part comprises alternatively clockwise and counter-clockwise with opposite magnetization directions that are sandwiched between stator cores. To provide path to working flux, the magnetization direction of the PMs in the inner and outer armature are in opposite directions. The magnetization direction, along with the flux path direction, is shown in Figure. 3(a). It can be seen that the flux generated from the inner armature PMs link with the rotor through the inner air gap and then enter to outer armature through the outer air gap. The flux in the outer armature passes again to the rotor through the outer air-gap and links with the inner armature through the inner air-gap to complete the magnetic circuit. Overall, a series magnetic circuit is formed to complete one flux path.

In comparison with DSCR-PMFSG, the proposed DRCR-PMFSG is comprised of one stator and two rotors. The rotors are located in the inner and outer regions, sharing one common stator. The stator of the proposed DRCR-PMFSG is encompassed alternatively opposite and circumferentially magnetized PMs sandwich between the armature winding of the upper slots and lower slots. Moreover, both the upper and lower slots are split through a flux bridge that plays a major role in providing alternate flux paths to complete the magnetic circuit path. The flux path of the proposed DRCR-PMFSG is shown in Figure. 3(b). This flux path is verified utilizing finite element analysis (FEA) based JMAG designer v.20.1 as shown in Figure.4. It can be seen that delegated flux bridges play a vital role in the flux path. The inner rotor's flux enters the inner armature portion through the inner air-gap that flows through the flux bridge and then enters the inner rotor through the inner air-gap at an alternate pole to complete the magnetic circuit.

Similarly, the magnetic flux path of the outer rotor also completed. Comparing the magnetic flux path of DSCR-PMFSG and proposed DRCR-PMFSG, it can be seen that DRCR-PMFSG complete magnetic circuits with two

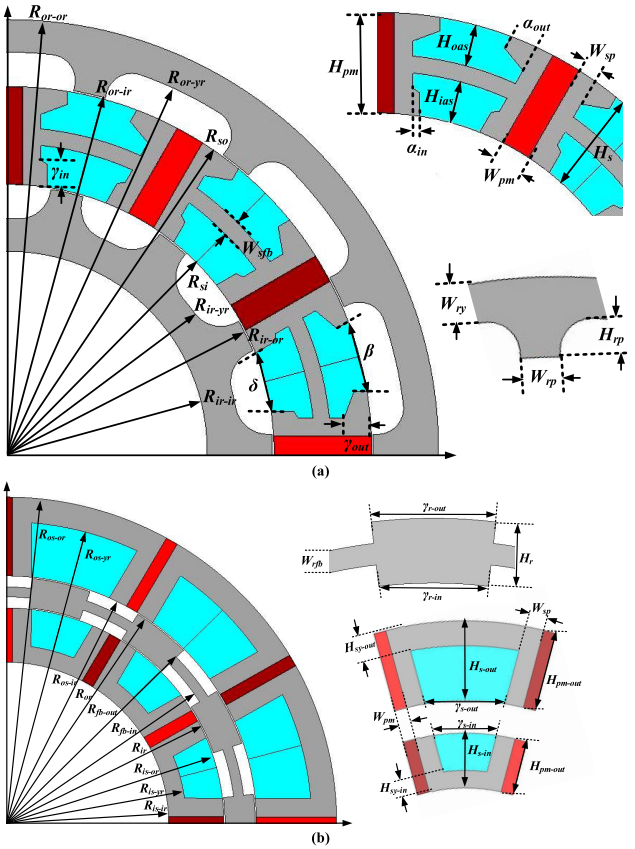

FIGURE 5. Illustration of design specification of (a) proposed DRCR-PMFSG and (b) conventional DSCR-PMFSG.

parallel magnetic paths. The magnetic flux of the inner and outer rotor superimposes the generated flux, resulting in better flux modulation and enhanced output power capability to almost two times. Thus, using the same magnetic loading, the proposed DRCR-PMFSG offers almost double output power and higher torque density than the conventional DSCR-PMFSG.

Design concept and modeling of conventional DSCR-PMFSG along with key design parameters can be addressed in [38], [39], whereas for proposed DRCR-PMFSG, stator slot (N_s) and rotor pole (N_r) combination for the inner and outer rotor are calculated as [40]

$$N_s = 2mn_1 \quad (n_1 = 1, 2, 3 \ldots) \tag{1}$$

$$N_r = N_s \pm n_2 \quad (n_2 = 1, 2, 3 \ldots) \tag{2}$$

where m is the number of phases, n_1 is integer number when m is even number but n_1 should be an even number in the case when m is odd number because the number of stator pole must be even.

Based on N_r and generator speed (n), no-load back-EMF frequency can be expressed as [41]

$$f = \frac{N_r n}{60} \tag{3}$$

A reduced number of rotor poles is preferred for reduced iron losses, whereas reduced pole number causes a reduction

TABLE 1. Design Specification of Proposed DRCR-PMFSG and Conventional DSCR-PMFSG.

DRCR-PMFSG		DSCR-PMFSG	
Symbol	Values	Symbol	Values
R_{or-or}	132 mm	R_{is-ir}	65 mm
R_{or-ir}	112 mm	R_{is-yr}	72 mm
R_{or-yr}	122 mm	R_{is-or}	87 mm
R_{so}	111.5 mm	R_{ir}	87.5 mm
R_{si}	81.5 mm	R_{fb-in}	91.5 mm
R_{ir-or}	81 mm	R_{fb-out}	95.5 mm
R_{ir-ir}	61 mm	R_{or}	99.5 mm
R_{ir-yr}	71 mm	R_{os-ir}	100 mm
W_{ry}	10 mm	R_{os-yr}	122 mm
H_{rp}	10 mm	R_{os-or}	132 mm
W_{rp}	10 mm	H_{pm-in}	22 mm
W_{pm}	9 mm	W_{pm}	5 mm
H_{pm}	30 mm	H_{pm-out}	32 mm
W_{sfb}	5 mm	H_{s-out}	32 mm
W_{sp}	5.5 mm	H_{s-in}	22 mm
H_{ias}	12.5 mm	H_{sy-out}	10 mm
H_{oas}	12.5 mm	H_{sy-in}	7 mm
α_{in}	2 mm	γ_{s-in}	24.4 mm
α_{out}	8 mm	γ_{s-out}	32.2 mm
γ_{in}	8 mm	W_{sp}	7.5 mm
γ_{out}	8 mm	γ_{r-in}	20 mm
δ	18.5 mm	γ_{r-out}	23 mm
β	20 mm	W_{rfb}	4 mm
N_c	100	H_r	12 mm
		N_c	100

in phase back-EMF frequency. Considering a compromise between high back-EMF and low-frequency operation, initially design with 12 stator slots and 14 poles (12S-14P) is chosen.

Design specification of the proposed DRCR-PMFSG is shown in Figure. 5, where leading design parameters are marked. Since the proposed DRCR-PMFSG shares one stator portion with both inner and outer rotor, some geometric parameters will be shared. Therefore, sizing equations accounts for both specific and shared geometric parameters. Based on required rated voltage (V_r), phase current (I_r), efficiency (η), and power factor, the output power (P_{out}) is expressed as

$$P_{out} = mV_rI_r\eta cos\varphi \tag{4}$$

For PMFSMs, approximate sinusoidal induced back-EMF is

$$e = -N_c\omega\phi_{max}\cos(\omega t) \tag{5}$$

$$\omega = 2\pi nN_r \tag{6}$$

Whereas N_c and ϕ_{max} are number of turns per phase and maximum air-gap flux density and can be expressed as

$$N_c = \frac{N_sE}{\sqrt{2}n\pi^2k_LN_rD_g^2B_{g-max}} \tag{7}$$

$$\phi_{max} = B_{g-max}A_{coil} \tag{8}$$

Whereas E is rms induced phase back-EMF, k_L is aspect ratio and D_g is air-gap diameter and expressed as

$$E = \frac{2n\pi^2N_cN_rL_sD_gB_{g-max}}{\sqrt{2}N_s} \tag{9}$$

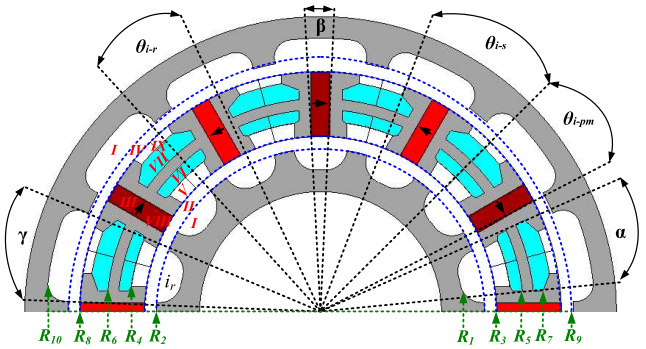

FIGURE 6. Sub-domain regions and interface conditions.

$$k_L = \frac{L_s}{D_g} \tag{10}$$

$$D_g = \sqrt[3]{\frac{P_{out}N_s}{\sqrt{2}\pi^3\eta nN_rA_sB_{g-max}k_Lk_E\cos(\phi)}} \tag{11}$$

Whereas A_s and L_s is electric loading and active stack length.

Thus, sub-optimal design parameters of the proposed CR-DRPMFSG such as outer radius of the outer rotor, the outer radius of inner rotor, stator outer radius, PM height, stator height, the width of the stator flux bridge is expressed as

$$R_{or-or} = R_{ir-ir} + R_{ir-or} + 2D_g + R_{so} + R_{or-ir} \tag{12}$$

$$R_{ir-or} = R_{ir-ir} + W_{ry} + H_{rp} \tag{13}$$

$$R_{so} = R_{ir-ir} + W_{ry} + H_{rp} + D_g + H_s \tag{14}$$

$$H_{pm} = H_{ias} + W_{sfb} + H_{oas} \tag{15}$$

$$H_s = H_{ias} + W_{sfb} + H_{oas} \tag{16}$$

$$W_{sfb} = (R_{so} - H_{oas}) - (R_{si} + H_{ias}) \tag{17}$$

Whereas based on the general design rule of permanent magnet flux switching machines, initially stator tooth width, rotor pole width, stator opening for inner and outer armature winding, and PM width are assumed to be equal [42].

To account for saturation effects, improve torque calculation, and reduce slotting effects that cause cogging torque in the air-gap, optimum design parameters are investigated utilizing finite element analysis (FEA). The final optimum design parameters of proposed DRCR-PMFSG and conventional DSCR-PMFSG were obtained based on FEA using built-in genetic optimization of JMAG designer v.20.1 as listed in Table. 1, which is used for detailed performance analysis of the DRCR-PMFSG.

IV. SUB-DOMAIN MODEL

Magnetic field distribution of electric machines is widely investigated utilizing Finite Element Analysis (FEA) based numerical techniques and analytical techniques i.e., conformal mapping [43], magnetic equivalent circuit (MEC) [44], lumped parameter MEC (LPMEC) [45], relative air-gap permeance calculation [46] and sub-domain model (SDM) [8].

Based on comparative analysis of analytical techniques, SDM is found to be more accurate than other analytical techniques [7]. SDM is widely adopted in permanent magnet permanent magnet synchronous machine [47], [48], consequent-pole flux switching machines [5], [7], [8], vernier machines [49], and inner/outer rotor flux switching machines [50] however, to the best of author knowledge, no reference in literature reporting SDM in dual rotor permanent magnet flux switching machines (DRPMFSM) are reported. Therefore, this section focusses on development of SDM based on Laplace and Poisson equations accounting magnetic saturation, slotting effects, winding configuration and magnetization orientation.

In SDM, the proposed DRCR-PMFSG overall model is divided into nine sub-domain regions (as shown in Figure. 6) which includes inner/outer rotor slot region (Domain I), inner air-gap region (Domain II), stator permanent magnet region (Domain III), outer air-gap region (Domain IV), inner stator slot-opening (Domain V), inner stator slot region (Domain VI), outer stator slot region (Domain VII), Permanent magnet opening (Domain VIII), and outer stator slot-opening (Domain IX).

Each of the aforesaid sub-domain regions are solved for magnetic vector potential utilizing Laplace and Poisson equations in polar forms. Generally, Laplace equation are expressed as [51]

$$\frac{\partial^2 A}{\partial r^2}+\frac{1}{r}\frac{\partial A}{\partial r}+\frac{1}{r^2}\frac{\partial^2 A}{\partial \theta^2}=0\begin{cases}R_1\le r\le R_2\\ \theta_1\le\theta\le\theta_2\end{cases} \tag{18}$$

Simplifying by replace r with R_1e^{-t}, we have

$$\frac{\partial^2 A}{\partial t^2}+\frac{\partial^2 A}{\partial \theta^2}=0\begin{cases}\ln(R_1/R_2)\le t\le 0\\ \theta_1\le\theta\le\theta_2\end{cases} \tag{19}$$

Since overall machine is modeled into nine sub-domain regions, magnetic potential of each region is computed one by one. Utilizing Laplace and Poisson equation, magnetic vector potential in domain I to domain IX are computed as

$$\begin{aligned}&\textit{Domain I}\\ &\textit{inner rotor}\end{aligned}:\frac{\partial^2 A_I}{\partial t^2}+\frac{\partial^2 A_I}{\partial \theta^2}=0\begin{cases}\ln(R_1/R_2)\le t\le 0\\ \theta_{i-r}\le\theta\le\theta_{i-r}+\gamma\end{cases} \tag{20}$$

$$\begin{aligned}&\textit{Domain I}\\ &\textit{Outer rotor}\end{aligned}:\frac{\partial^2 A_I}{\partial t^2}+\frac{\partial^2 A_I}{\partial \theta^2}=0\begin{cases}\ln(R_8/R_9)\le t\le 0\\ \theta_{i-r}\le\theta\le\theta_{i-r}+\gamma\end{cases} \tag{21}$$

$$\textit{Domain II}:\frac{\partial^2 A_{II}}{\partial t^2}+\frac{\partial^2 A_{II}}{\partial \theta^2}=0\begin{cases}\ln(R_2/R_3)\le t\le 0\\ \theta_i\le\theta\le\theta_i+\gamma\end{cases} \tag{22}$$

$$\textit{Domain III}:\frac{\partial^2 A_{III}}{\partial t^2}+\frac{\partial^2 A_{III}}{\partial \theta^2}=-\mu_o\frac{M_\theta}{r}\begin{cases}\ln(R_3/R_8)\le t\le 0\\ \theta_{i-pm}\le\theta\le\theta_{i-pm}+\gamma\end{cases} \tag{23}$$

$$\textit{Domain IV}:\frac{\partial^2 A_{IV}}{\partial t^2}+\frac{\partial^2 A_{IV}}{\partial \theta^2}=0\begin{cases}\ln(R_8/R_9)\le t\le 0\\ \theta_{i-r}\le\theta\le\theta_{i-r}+\gamma\end{cases} \tag{24}$$

$$\textit{Domain V}:\frac{\partial^2 A_V}{\partial t^2}+\frac{\partial^2 A_V}{\partial \theta^2}=0\begin{cases}\ln(R_3/R_4)\le t\le 0\\ \theta_{i-s}\le\theta\le\theta_{i-s}+\alpha\end{cases} \tag{25}$$

$$\textit{Domain VI}:\frac{\partial^2 A_{VI}}{\partial t^2}+\frac{\partial^2 A_{VI}}{\partial \theta^2}=-\mu_o J\begin{cases}\ln(R_4/R_5)\le t\le 0\\ \theta_{i-s}\le\theta\le\theta_{i-s}+\alpha\end{cases} \tag{26}$$

$$\textit{Domain VII}:\frac{\partial^2 A_{VII}}{\partial t^2}+\frac{\partial^2 A_{VII}}{\partial \theta^2}=-\mu_o J\begin{cases}\ln(R_6/R_7)\le t\le 0\\ \theta_{i-s}\le\theta\le\theta_{i-s}+\alpha\end{cases} \tag{27}$$

$$\textit{Domain VIII}:\frac{\partial^2 A_{VIII}}{\partial t^2}+\frac{\partial^2 A_{VIII}}{\partial \theta^2}=0\begin{cases}\ln(R_3/R_4)\le t\le 0\\ \theta_{i-s}\le\theta\le\theta_{i-s}+\alpha\end{cases} \tag{28}$$

$$\textit{Domain IX}:\frac{\partial^2 A_{IX}}{\partial t^2}+\frac{\partial^2 A_{IX}}{\partial \theta^2}=0\begin{cases}\ln(R_7/R_8)\le t\le 0\\ \theta_{i-s}\le\theta\le\theta_{i-s}+\alpha\end{cases} \tag{29}$$

General solution of the magnetic vector potential of the all the domains are obtained by solving Laplace and Poisson equations using boundary and interface conditions considering magnetic vector potential continuity using variable separation methods.

A. BOUNDARY CONDITIONS

Boundary conditions are defined to compute vector potential function for all sub-domain regions. Inner and outer rotor slots (Domain I) and its associated bottom are covered with lamination core where tangential magnetization is zero and the boundary conditions are represented as

$$\begin{cases}\left.\dfrac{\partial A_I}{\partial\theta}\right|_{\theta=\theta_{i-r}}=0\\ \left.\dfrac{\partial A_I}{\partial\theta}\right|_{\theta=\theta_{i-r}+\gamma}=0\\ \left.\dfrac{\partial A_I}{\partial\theta}\right|_{\theta=0}=0\end{cases} \tag{30}$$

Radial magnetic field component between inner air-gap and PM regions based on continuity of tangential magnetic field intensity leads to boundary condition as

$$\begin{cases}\left.\dfrac{\partial A_I}{\partial r}\right|_{r=R_3}=\dfrac{1}{\mu_o}\left.\dfrac{\partial A_{III}}{\partial r}\right|_{r=R_3}\\ \left.\dfrac{\partial A_I}{\partial\theta}\right|_{r=R_3}=\dfrac{1}{\mu_o}\left.\dfrac{\partial A_{III}}{\partial\theta}\right|_{r=R_3}\end{cases} \tag{31}$$

Similarly, radial magnetic field component between outer air-gap and PM regions based on continuity of tangential

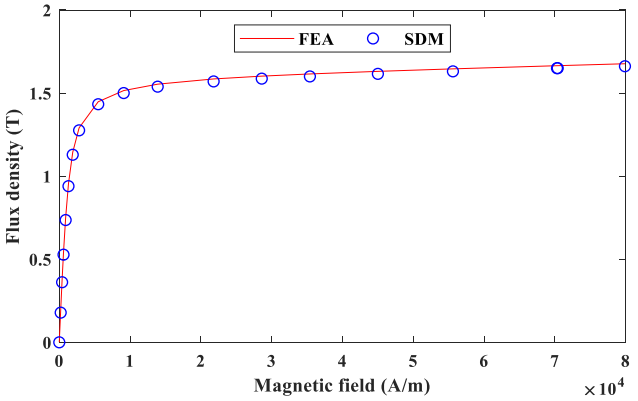

FIGURE 7. B-H magnetization curve.

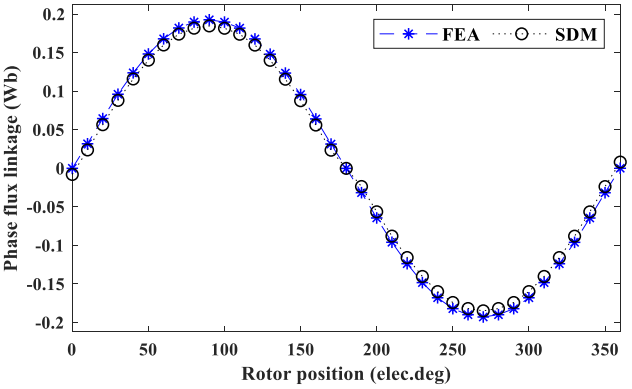

FIGURE 8. Validation of phase flux linkage.

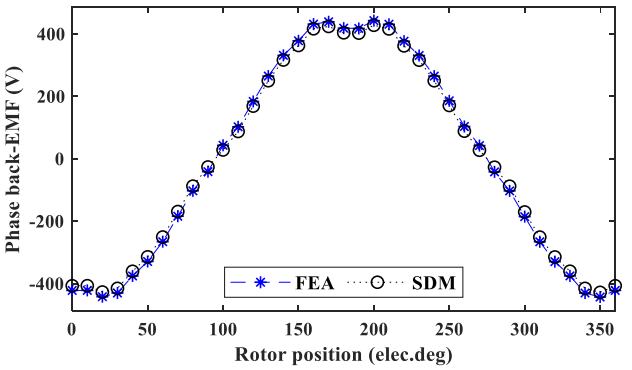

FIGURE 9. Comparison of phase back-EMF.

magnetic field intensity leads to boundary condition as

$$\begin{cases} \left.\dfrac{\partial A_I}{\partial r}\right|_{r=R_8} = \dfrac{1}{\mu_o}\left.\dfrac{\partial A_{III}}{\partial r}\right|_{r=R_8} \\ \left.\dfrac{\partial A_I}{\partial \theta}\right|_{r=R_8} = \dfrac{1}{\mu_o}\left.\dfrac{\partial A_{III}}{\partial \theta}\right|_{r=R_8} \end{cases} \tag{32}$$

Stator are composed of lamination core material in which the flux flow and ultimately current flows, Therefore, boundary conditions between inner/outer air-gap and stator core is given by

$$\begin{cases} \left.\dfrac{\partial A_I}{\partial r}\right|_{r=R_3} = \mu_o J|_{r=R_3} \\ \left.\dfrac{\partial A_I}{\partial r}\right|_{r=R_8} = \mu_o J|_{r=R_8} \end{cases} \tag{33}$$

B. STATOR SLOT AND ROTOR POLE COMBINATION

In the aforesaid sub-domain regions, rotor slot opening, stator slot opening, and permanent magnet opening are represented as γ, α, and β, respectively which varies with the rotor pole number, stator slot and number of PM being used. These angular position of the i_r^{th} rotor slots, i_s^{th} stator slot and i_{pm}^{th} permanent magnet with respect to variation of the rotor poles and stator slots combination is expressed as

$$\theta_{i-r} = -\frac{\gamma}{2} + \frac{2i_r\pi}{N_r} + \theta_{ro} \quad for\ 1 \le i_r \le N_r \tag{34}$$

$$\theta_{i-s} = -\frac{\alpha}{2} + \frac{2i_s\pi}{N_s} + \theta_{so} \quad for\ 1 \le i_s \le N_s \tag{35}$$

$$\theta_{i-pm} = -\frac{\beta}{2} + \frac{2i_{pm}\pi}{N_{pm}} + \theta_{pmo} \quad for\ 1 \le i_{pm} \le N_{pm} \tag{36}$$

C. MAGNETIC SATURATION

Permeability of the rotor and stator core differs with operating points and behave in non-linear forms therefore, effects accuracy of the analytical model due to magnetic saturation. Thus, to account the effects of magnetic saturation, permeability of the core material required to be updated through iterative process. Therefore, an exact relation between flux density and field intensity (B-H curve) is required for computation of magnetic reluctance of core material. An approximates magnetization curve can be expressed as

$$B_i(H_i) = \mu_o\left\{H_i + M_s\left(\coth\left(\frac{H_i}{\delta}\right) - \left(\frac{\delta}{H_i}\right)\right)\right\} \tag{37}$$

Whereas M_s and δ are saturation magnetization and material coefficient, respectively. B_i and H_i are magnetic flux density and field intensity, respectively for the core material which is computed through iterative process.

Magnetic field intensity in core material (rotor/stator) are computed as

$$H_i^{n-1} = \frac{\Delta F_i^{n-1}}{l} \tag{38}$$

Whereas ΔF_i^{n-1} is node magnetic potential drop and l is length of the core material.

Based on ΔF_i^{n-1}, permeability of core is updated in accordance with the magnetization curve as

$$\mu_r^n = \frac{\left\{H_i^{n-1} + M_s\left(\coth\left(\frac{H_i^{n-1}}{\delta}\right) - \frac{\delta}{H_i^{n-1}}\right)\right\}}{H_i^{n-1}} \tag{39}$$

This process is repeated in iterative process by updating μ_r until precise B_i^n and H_i^n are obtained where B_i^n is obtained as

$$B_i^n = \Delta F_i^n \frac{P}{A} \tag{40}$$

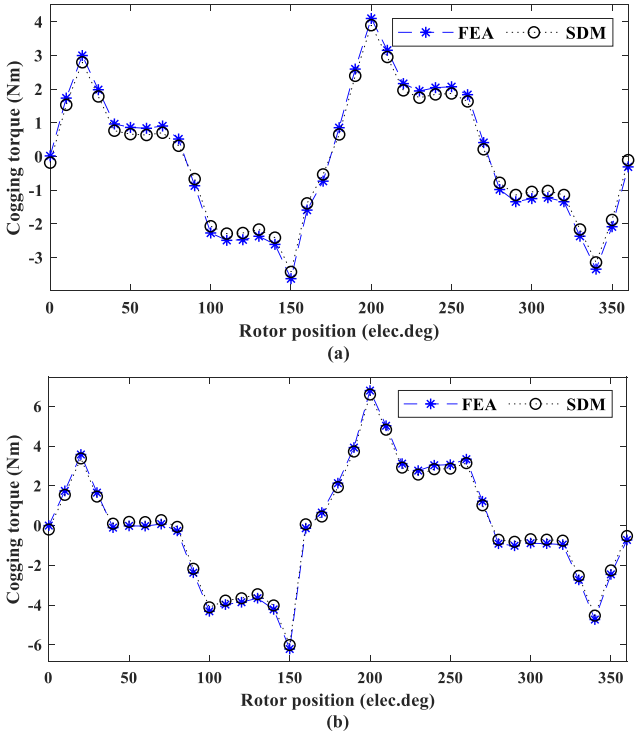

FIGURE 10. Validation of cogging torque (a) inner rotor and (b) outer rotor.

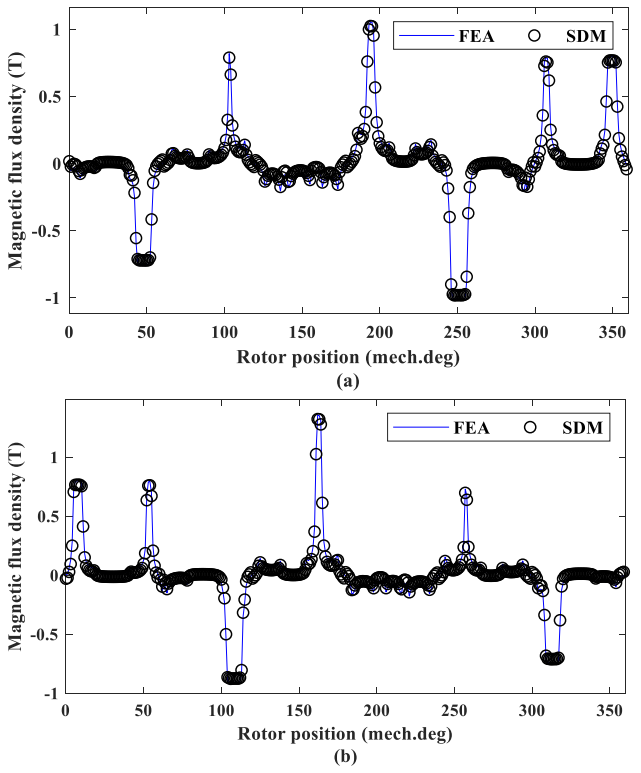

FIGURE 11. Validation of magnetic flux density (a) Inner rotor and (b) Outer rotor.

After several iterations, B-H magnetization curved of the core material obtained as shown in Figure. 7.

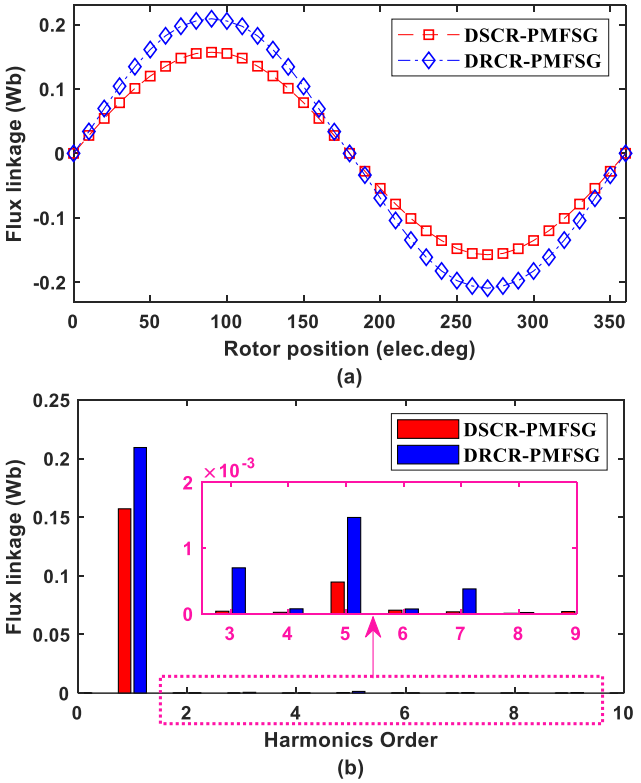

FIGURE 12. Flux linkage (a) waveform and (b) harmonic spectra.

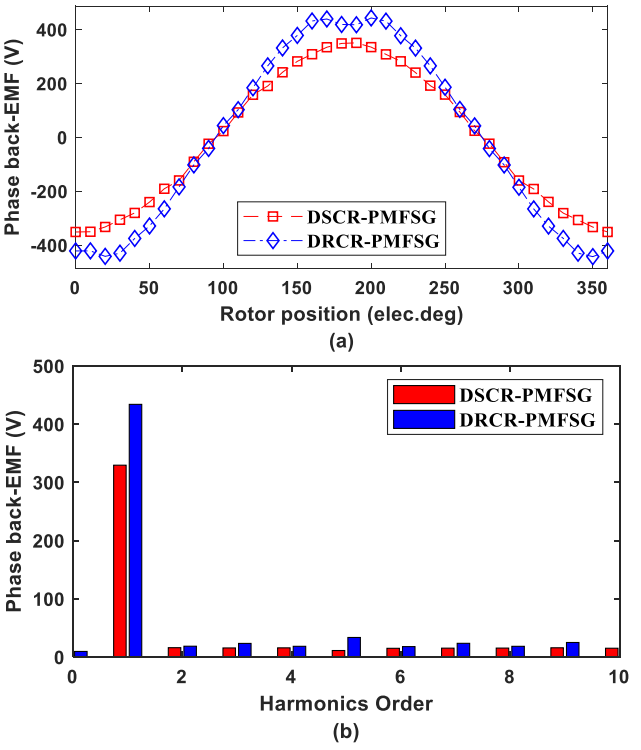

FIGURE 13. Open-circuit phase back-EMF (a) waveform and (b) harmonic spectra.

D. WINDING CONFIGURATION

By varying the winding configuration, the phase flux vector varies. This phase flux vector in case of single layer winding

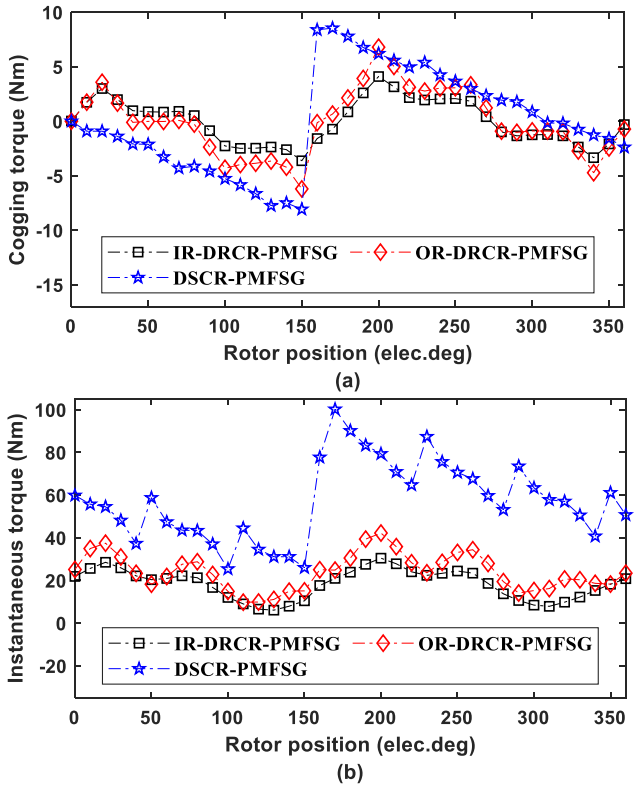

FIGURE 14. Torque performance (a) cogging torque and (b) instantaneous torque.

connection is expressed as

$$\begin{bmatrix} \psi_a \\ \psi_b \\ \psi_c \end{bmatrix} = N_c C^T \begin{bmatrix} \phi_1 & \phi_2 & \phi_3 & \dots & \phi_{N_s} \end{bmatrix} \quad (41)$$

Whereas C and ϕ are matrix connection and slot flux. The inner and outer stator slot flux are computed as

$$\phi_{inner} = -\frac{R_4^2 L_s}{A k_f} \int_0^{\beta} \int_0^{\ln(R_4/R_5)} e^{-2t} A_{VIi}(t,\theta) dt d\theta \quad (42)$$

$$\phi_{outer} = -\frac{R_4^2 L_s}{A k_f} \int_0^{\beta} \int_0^{\ln(R_6/R_7)} e^{-2t} A_{VIIi}(t,\theta) dt d\theta \quad (43)$$

Whereas A and k_f are slot area and filling factor.

In case of double layer winding, the phase flux vector is computed as

$$\begin{bmatrix} \psi_a \\ \psi_b \\ \psi_c \end{bmatrix} = \frac{N_c}{2} \left\{ \begin{array}{l} C_1^T \begin{bmatrix} \phi_{1i} & \phi_{1i} & \phi_{1i} & \dots & \phi_{N_s} \end{bmatrix} \\ + C_2^T \begin{bmatrix} \phi_{2i} & \phi_{2i}\phi & {}_{2i} & \dots & \phi_{N_s} \end{bmatrix} \\ for\ i = 1, 2 \dots \end{array} \right\} \quad (44)$$

Whereas

$$\phi_{inner} = -\frac{2R_4^2 L_s}{A k_f} \int_0^{\beta/2} \int_0^{\ln(R_4/R_5)} e^{-2t} A_{VIi}(t,\theta) dt d\theta \quad (45)$$

$$\phi_{outer} = -\frac{2R_4^2 L_s}{A k_f} \int_0^{\beta/2} \int_0^{\ln(R_6/R_7)} e^{-2t} A_{VIIi}(t,\theta) dt d\theta \quad (46)$$

E. PERFORMANCE ANALYSIS

Based on air-gap magnetic flux density, back-EMF waveform is computed utilizing Faraday's Law as

$$E_c(t) = -N_c \frac{d\psi}{dt} \quad (47)$$

The phase flux is computed as

$$\psi(t) = L_s R \int_0^{2\pi} B_{IIr}(t,\theta) d\theta \quad (48)$$

Finally, using radial (B_r) and tangential (B_θ) magnetic flus density components, cogging torque are obtained as

$$T = \frac{L_s}{\mu_o} \int_0^{2\pi} B_r(t,\theta) B_\theta(t,\theta) d\theta \quad (49)$$

Whereas

$$\begin{cases} B_r^i = \dfrac{1}{r} \dfrac{\partial A_i}{\partial \theta} \\ B_\theta^i = -\dfrac{\partial A_i}{\partial \theta} \\ for\ i = II, IV \end{cases} \quad (50)$$

The developed SDM is validated by comparing performance analysis such as phase flux linkage, back-EMF, cogging torque and magnetic flux density obtained through FEA and analytical method as shown in Figure. 8 to Figure. 11. It can be clearly seen that developed SDM fairly match FEA.

V. STATIC ANALYSIS

This section investigated finite element analysis (FEA) based static performance of conventional DSCR-PMFSG and proposed DRCR-PMFSG. Static performance is obtained under open-circuit analysis and brushless AC operation. Under open-circuit conditions, phase flux linkage, back-EMF, and cogging torque are obtained, whereas instantaneous torque is obtained under brushless AC operation. Detailed performance of conventional DSCR-PMFSG and proposed DRCR-PMFSG is illustrated in Figure. 12-14.

FEA-based open circuit analysis of the flux linkage waveform is shown in Figure. 12(a) and harmonic spectra in Figure. 12(b). Quantitative analysis reveals that the maximum peak flux linkage offered by DSCR-PMFSG is 0.1571 Wb. In contrast, the proposed DRCR-PMFSG offers 0.2094 Wb with the peak-to-peak flux of 0.3142 Wb by DSCR-PMFSG and 0.4188 Wb DRCR-PMFSG, which is mainly due to improved flux path and dominant high fundamental component and lower higher-order harmonics content contributing to the fundamental component. It can be clearly seen that in the case of counter-rotation with the proposed dual rotor configuration, the magnitude of the flux

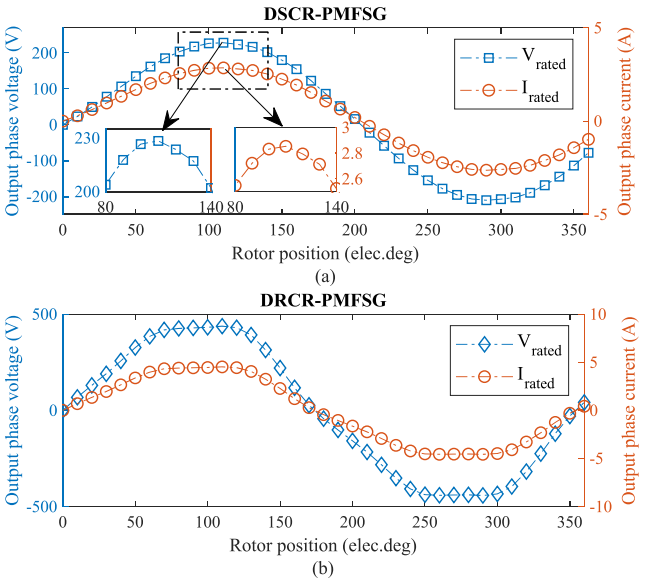

FIGURE 15. Output phase current and phase voltage at rated condition (a) DSCR-PMFSG and (b) DRCR-PMFSG.

linkage increases by 33.29%. Therefore, due to higher phase flux, the induced back-EMF is also improved, as shown in Figure. 13(a). In open-circuit analysis, back-EMF is induced at the open winding terminals when no source is applied to the armature winding. Quantitative analysis reveals that the maximum peak back-EMF offered by DSCR-PMFSG is 329.76 V whereas the proposed DRCR-PMFSG offers 433.858 V. The RMS value of 232.96 V is offered by DSCR-PMFSG and 306.73 V by DRCR-PMFSG. The improved back-EMF in the proposed DRCR-PMFSG is mainly due to higher flux and dominant higher fundamental component with additional higher-order harmonics content that contributes to the fundamental component, as shown in Figure. 13(b). Analysis reveals that in the proposed DRCR-PMFS, back-EMF is improved by 31.72%.

Flux modulation effect due to salient rotors structure shows major role in air-gap magnetic flux density where the field harmonics generated by PM and armature reaction rotates synchronously to generate the torque. Since the proposed DRCR-PMFSG configuration is associated with two mechanical ports, i.e., inner rotor (IR) and outer rotor (OR) therefore, the influence of both individual rotors on cogging torque and instantaneous torque are investigated in Figure. 14.

From Figure. 14(a), it can be clearly seen that the inner rotor of DRCR-PMFSG (IR-DRCR-PMFSG) offers peak to peak cogging torque of 7.73 Nm, whereas the outer rotor of DRCR-PMFSG offers 13.01 Nm and conventional DSCR-PMFSG exhibits 16.617 Nm. Quantitative analysis of DSCR-PMFSG with IR-DRCR-PMFSG reveals that in the proposed DRCR-PMFSG with an inner rotor, cogging torque is reduced by 53.48%. In contrast, in comparison with OR-DRCR-PMFSG, cogging torque is reduced by 21.7%. Therefore, the proposed DRCR-PMFSG offers low vibration and acoustic noise [52] and low torque ripples content in instantaneous torque, as seen in Figure. 14(b).

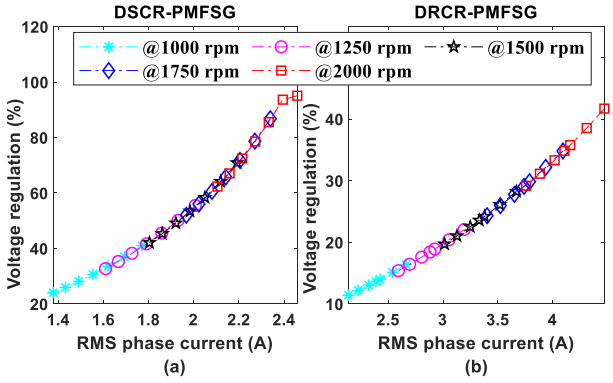

FIGURE 16. Voltage regulation factor in (a) DSCR-PMFSG and (b) DRCR-PMFSG.

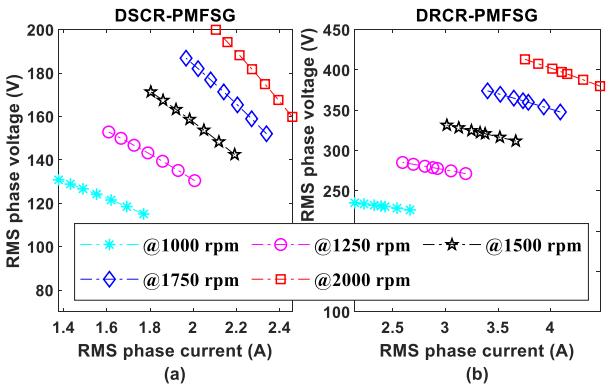

FIGURE 17. Output voltage response with output current for (a) DSCR-PMFSG and (b) DRCR-PMFSG.

Quantitative analysis of instantaneous torque reveals that IR-DRCR-PMFSG offers average torque of 18.36 Nm. In contrast, OR-DRCR-PMFSG exhibits an average torque of 23.87 Nm with a cumulative torque of 42.23 Nm in DRCR-PMFSG, whereas DSCR-PMFSG offered an average torque of 57.12 Nm, which is 35.25% higher at the cost of increased torque ripples. Because the torque ripples exhibited by DSCR-PMFSG is 74.85 Nm, whereas IR-DRCR-PMFSG displays torque ripples of 24.35 Nm and OR-DRCR-PMFSG shows torque ripples of 32.39 Nm. Detail comparison of torque ripples of DSCR-PMFSG with IR-PMFSG unveils that IR-DRCR-PMFSG offers 67.45% lower torque ripples, whereas comparison with OR-DRCR-PMFSG shows 56.72% reduced torque ripples.

VI. GENERATING POWER PERFORMANCE

Power generating performance of proposed DRCR-PMFSG and conventional DSCR-PMFSG includes output current, output voltage, output power, losses, efficiency, output power density, and voltage regulation capability under symmetrical external resistive load. Detailed analysis under-rated condition and combined overload and over-speed capability is performed.

A. RATED PERFORMANCE

Rated output phase voltage and phase current for DSCR-PMFSG is shown in Figure 15(a) whereas for proposed

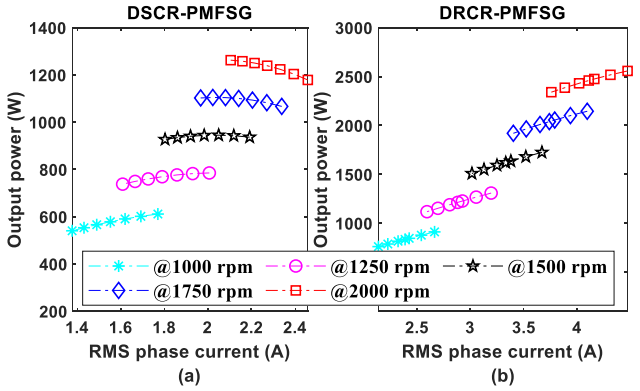

FIGURE 18. Analysis of output power with output current in (a) DSCR-PMFSG and (b) DRCR-PMFSG.

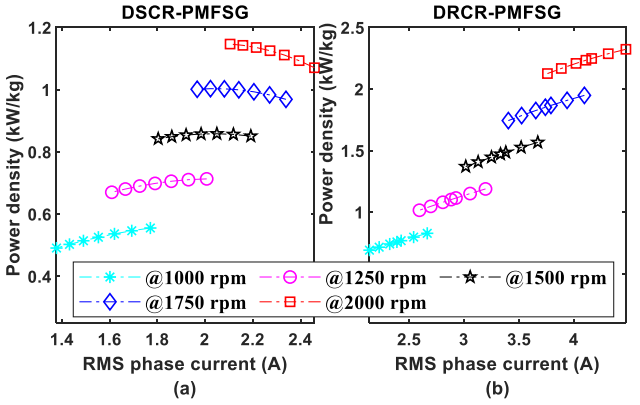

FIGURE 19. Behavior of output power density with output current in (a) DSCR-PMFSG and (b) DRCR-PMFSG.

DRCR-PMFSG cumulative (addition of both inner and outer armature port) voltage and current under rated conditions is shown in Figure. 15(b). Detailed analysis evident that conventional DSCR-PMFSG offer peak rated voltage of 228.3 V ($V_{rms} = 161.43V$) and peak rated current of 2.85 A ($I_{rms} = 2.02A$), whereas the proposed dual port DRCR-PMFSG, peak rated voltage of 199.75 V ($V_{rms} = 141.45V$) and peak rated current of 2.06 A ($I_{rms} = 1.46A$) are achieved at inner armature port whereas outer armature port offers peak rated voltage of 237.97 V ($V_{rms} = 168.27V$) and peak rated current of 2.45 A ($I_{rms} = 1.73A$). Analysis reveals that in comparison with conventional DSCR-PMFSG, cumulative voltage of 91.7% and cumulative current of 58.59% higher is achieved in proposed DRCR-PMFSG under rated operating condition. The improved voltage and current profile of the proposed DRCR-PMFSG are mainly due to dual flux modulation through stator flux bridge with the inner and outer rotor incorporating inner and outer armature which contributes to the cumulative output profile. In addition, rated operating power for DSCR-PMFSG is 973.42 W whereas for the proposed DRCR-PMFSG cumulative power (summation of inner and outer armature port power) is 1491.95 W. This shows that under the same specification, DRCR-PMFSG offer 1.53 times power than the counterpart DSCR-PMFSG. This is because inner armature port contributes 618.63 W and

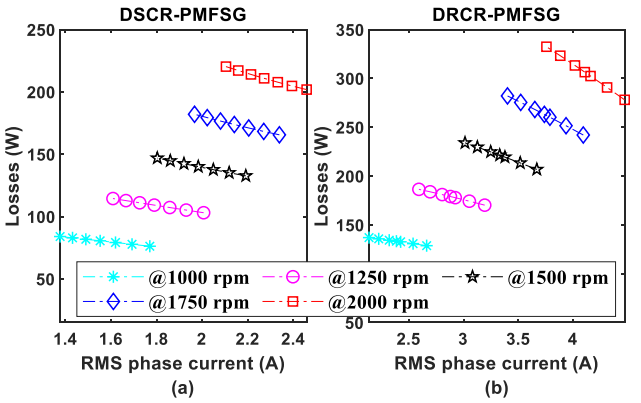

FIGURE 20. Influence of speed on losses in (a) DSCR-PMFSG and (b) DRCR-PMFSG.

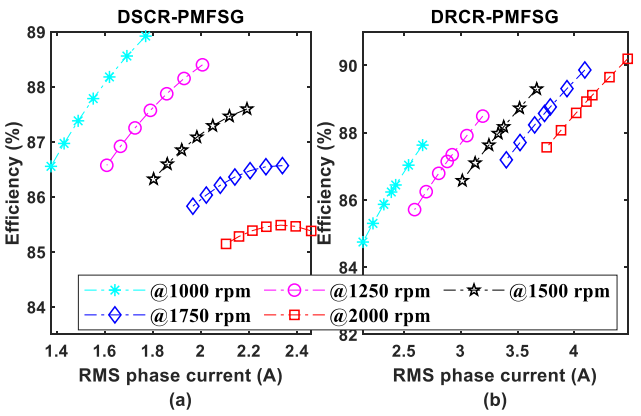

FIGURE 21. Variation of efficiency with speed in (a) DSCR-PMFSG and (b) DRCR-PMFSG.

outer armature contributes 873.32 W in cumulative output power of 1491.95 W that results an improved power. It is worth noting that flux linkages, back-EMF, output voltage, output current and generating power performance are illustrated and investigated as per cumulative response, not on individual port contribution.

B. OVERLOAD AND OVERSPEED CAPABILITY

This section coupled overload and over-speed capability for detailed investigation of generating power performance of both DSCR-PMFSG and DRCR-DRPMFSG, so that influence of the load variation with various speeds is analyzed in detail. In the case of over-speed capability, the design is operated at a higher speed than the rated. In contrast, in the case of the overload capability, a detailed investigation is performed on key performance indicators, i.e., voltage regulation, output current, output phase voltage, output power, power density, loss, and efficiency with various symmetrical, balanced three-phase resistive load. Voltage regulation is computed as [53]

$$U = \left(\frac{E_o}{U_o} - 1\right) 100\% \tag{51}$$

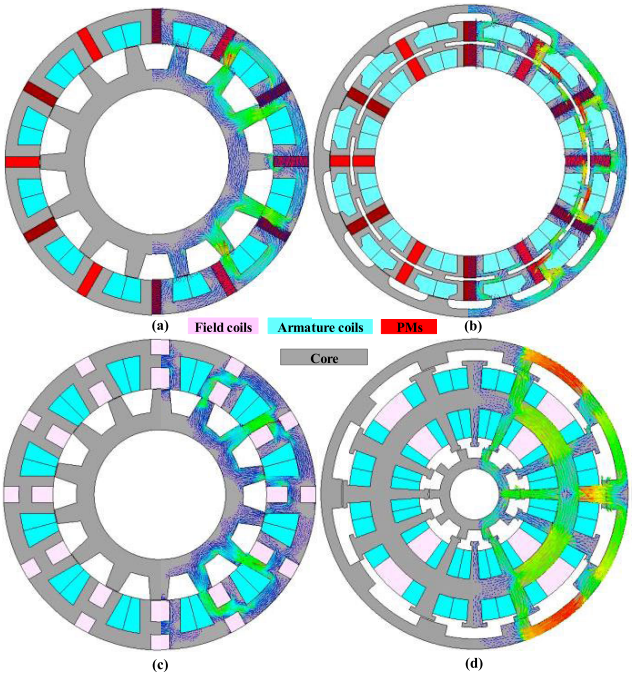

FIGURE 22. Cross sectional view of conventional (a) Inner rotor permanent magnet flux switching generator (b) Outer rotor permanent magnet flux switching generator (c) Inner rotor field excited flux switching generator and (d) Dual rotor field excited flux switching generator.

TABLE 2. Quantitative performance of conventional and proposed design.

DESIGNS	ψ_{pp} (Wb)	E_{MF} (V)	T_{cog} (Nm)	I_L (A)	V_L (V)	l_{osses} (W)
DRCR-PMFSG	0.39	292.69	7.73	**3.19**	**309.5**	221.34
DSCR-PMFSG	0.32	245.57	16.62	**2.01**	**161.43**	146.87
IR-PMFSG	0.17	133.36	9.27	1.31	129.52	222.38
OR-PMFSG	0.14	108.93	12.6	1.1	108.35	75.5
IR-FEFSG	0.25	133.46	0.27	1.3	87.76	25.19
DR-FEFSG	0.1	68.97	1.25	0.67	65.45	52.55

Whereas U_o is output load voltage and E_o is open-circuit back-EMF, which is computed as

$$\begin{cases} E_o = I_o\sqrt{\left(R_N + R_{ph}\right)^2 + X_s^2} \\ U_o = I_o R_N \end{cases} \tag{52}$$

Thus

$$U = \left(\frac{\sqrt{\left(R_N + R_{ph}\right)^2 + X_s^2}}{R_N} - 1\right) 100\% \tag{53}$$

Whereas R_N is connected resistive load, R_{ph} is phase winding resistance and X_s is winding synchronous reactance.

Figure. 16 shows a variation of the voltage regulation factor of conventional DSCR-PMFSG and proposed DRCR-PMFSG with output phase current and various operating speeds. It can be evident that with the increase in the rotational speed, the voltage regulation factor tends to rise due

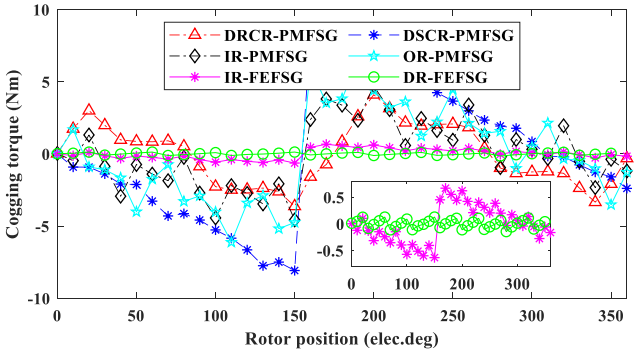

FIGURE 23. Cogging torque comparison between conventional and proposed design.

to the increase in the induced back-EMF and output voltage. However, analysis unveils that the growth rate of voltage regulation factor of DRCR-PMFSG is lower in comparison with the counterpart DSCR-PMFSG due to the distribution of mechanical output port that divides the overall voltage regulation factor to both the armature coils connected back-to-back in the stator slots and separated by flux bridge. In the case of DSCR-PMFSG the lowest voltage regulation factor of 24.04% is achieved at 1000 rpm whereas the highest voltage regulation factor of 95.08% at 2000 rpm whereas in the case of proposed DRCR-PMFSG, the lowest voltage regulation at 1000 rpm is 11.41%, and highest voltage regulation factor at 2000 rpm is 41.69%. Moreover, at the rated operating condition, DSCR-PMFSG exhibits 53.4% voltage regulation whereas 23.56% voltage regulation is obtained in proposed DRCR-PMFSG. A quantitative comparison of the conventional DSCR-PMFSG and proposed DRCR-PMFSG reveals that DRCR-PMFSG exhibits 55.88% improved voltage regulation factor, therefore, offers more stable voltage with the variation of the load changes. Moreover, RMS output voltage response with RMS output current of both DSCR-PMFSG and DRCR-PMFSG is shown in Figure. 17. At the lowest speed of 1000 rpm, DSCR-PMFSG offers an output voltage of 115.08 V, whereas DRCR-PMFSG exhibits an output voltage of 226.42 V that is 96.75% higher than its counterpart. Moreover, at a high-speed of 2000 rpm, DSCR-PMFSG shows an output voltage of 199.94 V, whereas 413.18 V is offered in the case of the proposed DRCR-PMFSG, which is 2.06 times the conventional DSCR-PMFSG. In addition, a comparison of the output voltage at rated operating conditions demonstrates 158.66V and 322.31V for conventional DSCR-PMFSG and DRCR-PMFSG, respectively. This analysis reveals that as soon as the rotational speed increases, the voltage drop rate in DSCR-PMFSG becomes higher in comparison with DRCR-PMFSG. It is evident that output voltages increase linearly with variation in speed with decreasing slop with a variation of the connected load. Output voltage stability under different resistive loads is analyzed from the curve slope. Analysis reveals that the slope of the curve for DRCR-PMFSG is higher than DSCR-PMFSG, thus indicating higher voltage variation with the resistive load variation,

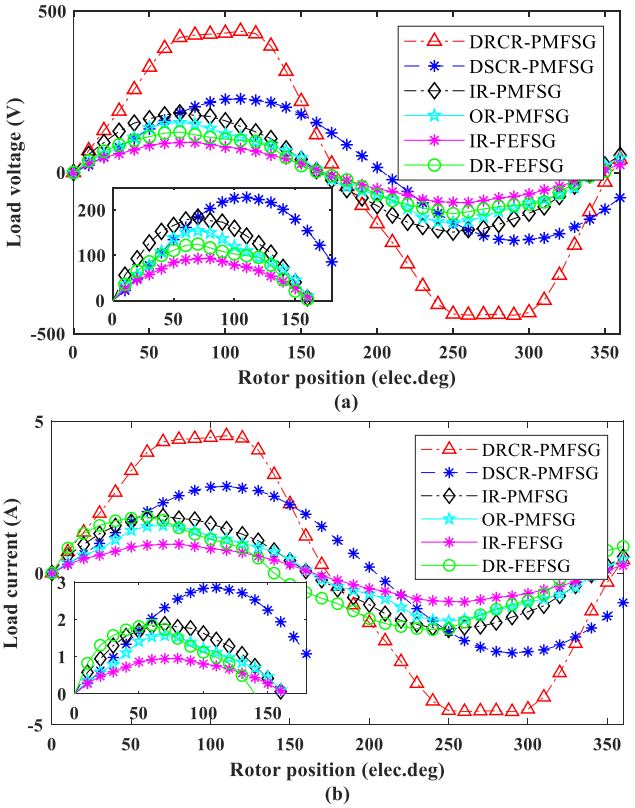

FIGURE 24. Conventional and proposed design output profile (a) load voltage and (b) load current.

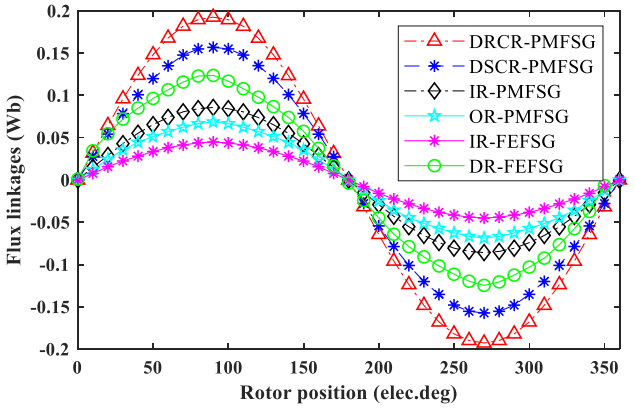

FIGURE 25. Phase flux linkage of conventional and proposed design.

therefore, exhibits advantages of maintaining more stable voltage. Output power and power density for DSCR-PMFSG and proposed DRCR-PMFSG are illustrated in Figure. 18 and Figure. 19, respectively. The analysis illustrates that conventional DSCR-PMFSG exhibits a good response in terms of the output power and power density till 1500 rpm, where the output power and corresponding power density increase with the increase in speed. When the rotational speed is increased further, the output power starts to saturate at 1750 rpm, and with the further increase in speed to 2000 rpm, the output power starts to decrease. In contrast, the output power and power density of the proposed DRCR-PMFSG

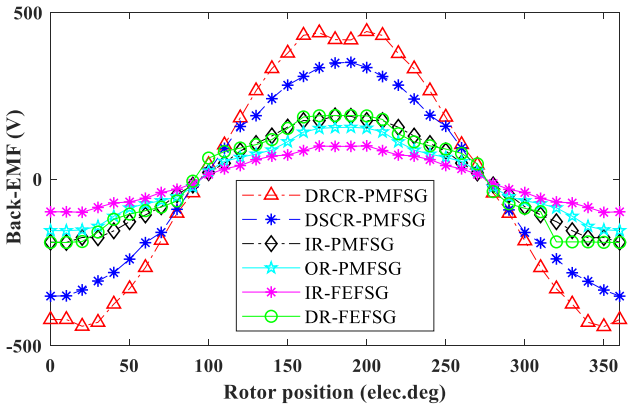

FIGURE 26. Back-EMF comparison of conventional and proposed design.

continue to increase with the increase in speed. Thus, it evident wide and high-speed operation capability of the proposed DRCR-PMFSG.

Quantitative comparative analysis of DSCR-PMFSG and DRCR-PMFSG unveil that proposed DRCR-PMFSG offer comparatively higher output power and power density. In rated operational conditions under low, medium, and high speed, conventional DSCR-PMFSG exhibits power density of 0.525, 0.857, and 1.125, respectively, whereas proposed DRCR-PMFSG offers 0.757, 1.47, and 2.23 power density, respectively. Analysis reveals that DRCR-PMFSG offers a power density of 1.44 times at low speed (@speed = 1000), which is amplified to 1.72 times at medium speed (@speed = 1500) and 1.98 times at higher speed (@speed = 2000). The main reason behind the improvement is that the growth rate of the power density lies in the output power curve that saturates in the case of DSCR-PMFSG and increases in the case of DRCR-PMFSG. This is because, stator is energetic part and consist of PMs and armature winding therefore, undergoes centrifugal force with rotation, causing dominant demagnetization of PM resulting saturation of the output curve. Finally, both DSCR-PMFSG and DRCR-PMFSG are investigated for losses and efficiency, as shown in Figure. 20 and Figure 21, respectively. Detailed investigation of loss for CR-DRPMFSG reveals that as soon as the connected load varies and rotational speed increases, corresponding losses tend to surge because of the rise in core losses due to elevation of frequency. Moreover, the variation of the losses under various speeds reveals that in the case of DSCR-PMFSG the losses continue to decline, but the decrement rate is slow compared to the proposed DRCR-PMFSG despite lesser overall losses. For conventional DSCR-PMFSG, at higher speed, the losses are high. In contrast, the corresponding output power also declines as the output power tends to saturate at medium speed and decline at a higher speed which greatly reduces efficiency at higher speed, as shown in Figure. 21(a). It is evident that for DSCR-PMFSG since the output power reduces with the speed and losses increase, the resultant efficiency continues to decrease at a higher speed. Therefore, DSCR-PMFSG offers maximum efficiency of 88.56% at a speed of 1000 rpm, whereas 88.08% efficiency is obtained

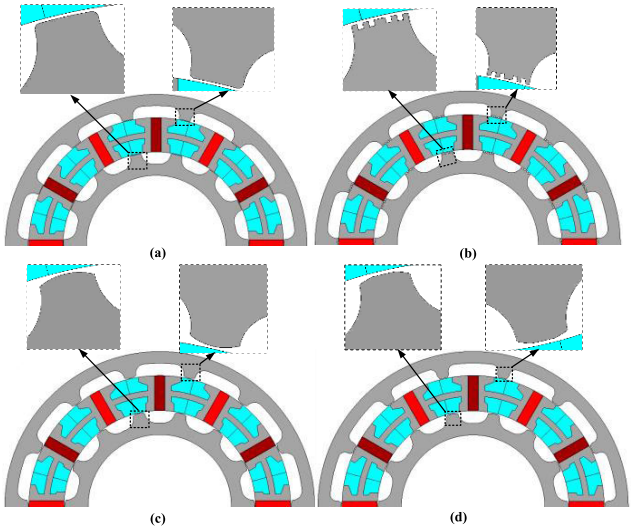

FIGURE 27. Rotor pole shaping (a) Chamfering (b) Notching (c) Eccentric circle and (d) sine shape.

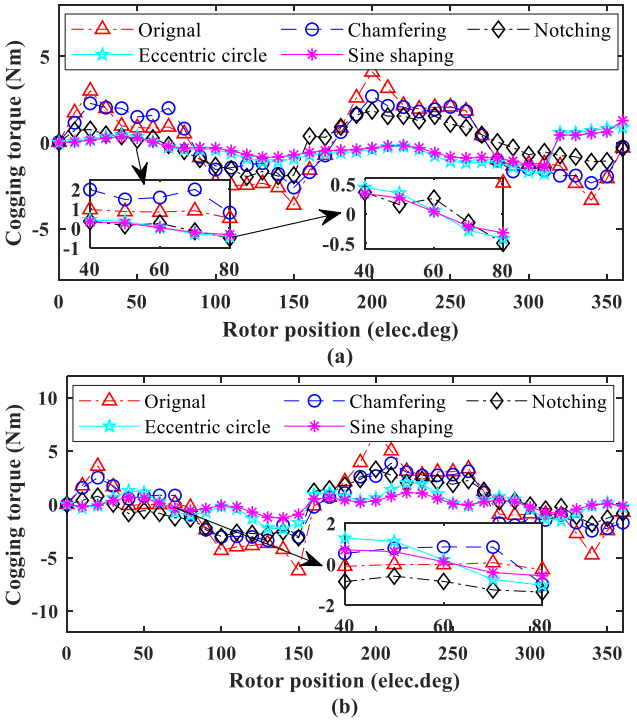

FIGURE 28. Cogging torque profile of (a) Inner rotor and (b) Outer rotor.

at rated operating conditions. In the case of the proposed DRCR-PMFSG, with the increase in the rotational speed, the corresponding output power tends to rise at a lower incremental rate of increase in the losses resulting in high efficiency at the high-speed region. The proposed DRCR-PMFSG offers the highest efficiency of 90.195% at a speed of 2000 rpm, whereas at rated operating condition of 1500 rpm, 87.98% efficiency is obtained is shown in Figure. 21.

VII. COMPARISON OF CONVENTIONAL AND PROPOSED DRCR-PMFSG

In order to evaluates effectiveness of proposed DRCR-PMFSG, detailed comparative analysis between proposed

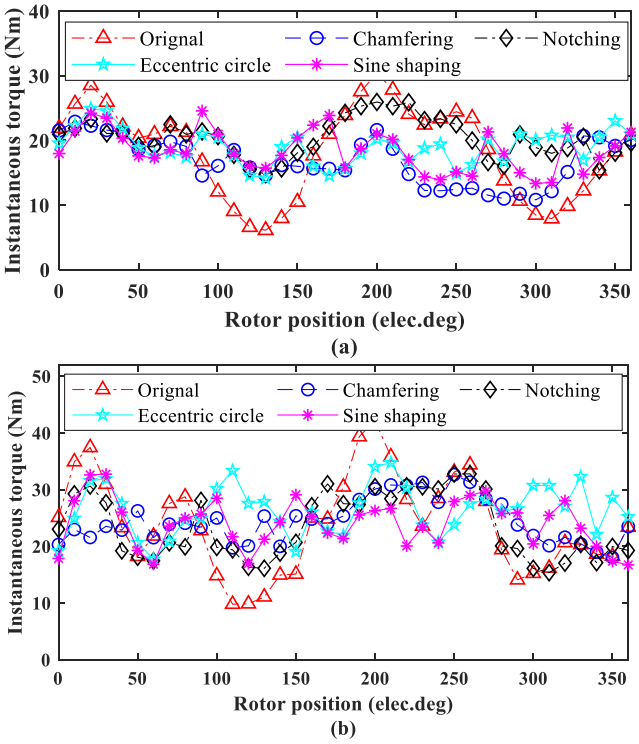

FIGURE 29. Instantaneous torque profile of (a) Inner rotor and (b) Outer rotor.

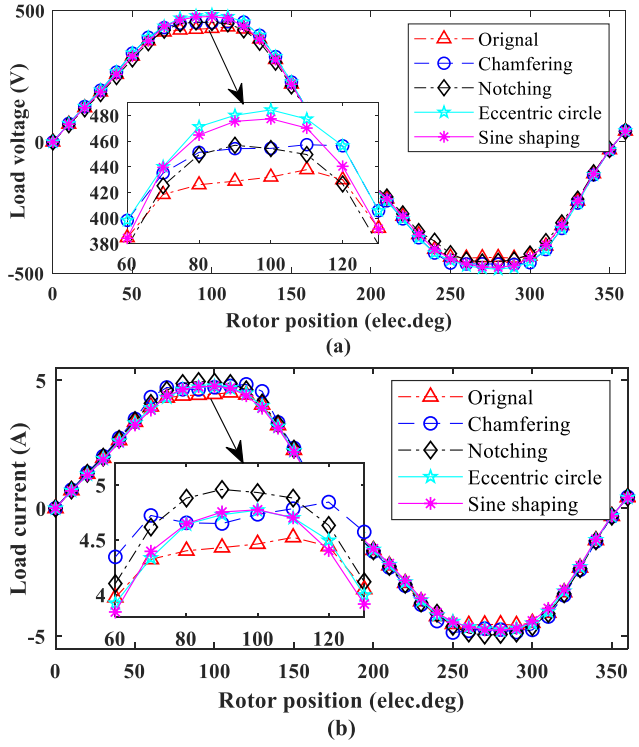

FIGURE 30. Load profile (a) output voltage and (b) output current.

design and conventional inner rotor PMFSG (IR-PMFSG) [54], outer rotor PMFSG (OR-PMFSG) [55], inner rotor field excited flux switching generator (IR-FEFSG) [56], and dual

rotor field excited flux switching generator (DR-FEFSG) [17] are investigated as shown in Figure. 22. A detailed quantitative performance analysis of proposed and conventional designs are listed in Table. 2 with key performance indicators i.e., phase flux linkage (ψ_{pp}), back-EMF (E_{MF}), cogging torque (T_{cog}), load current (I_L), load voltage (V_L) and losses (l_{osses}).

Based on comparative analysis it can be seen that both IR-FEFSG and DR-FESF topologies exhibit lower T_{cog} (as shown in Figure. 23) and losses than counterpart PM excited machines however, field excited machines offer lower load current and voltage (as shown in Figure. 24) resulting lower output power.

In case of PM excited machines, both IR-PMFSG and OR-PMFSG offers better performance than field excited machines but lower than DSCR-PMFG. Comparative study of conventional designs reveals that DSCR-PMFSG offer excellent performance among IR-PMFSG and OR-PMFSG however, in comparison with the proposed DRCR-PMFSG, conventional DSCR-PMFSG results lower output current and voltage that leads to reduced output power. Based on quantitative analysis, analysis unveil that proposed DRCR-PMFSG offer higher output power. Moreover, waveform of the phase flux linkage and back-EMF are shown in Figure. 25 and Figure. 26, respectively. It can be clearly seen that proposed DRCR-PMFSG exhibits highest phase flux linkage and back-EMF resembling sinusoidal waveform. From cogging torque waveform, it is found that proposed DRCR-PMFSG exhibits dominant cogging torque that results torque ripples in torque waveform.

This torque ripples are due to higher order harmonics especially 5th and 7th order harmonics in the back-EMF [57] which is replicated in output current and voltage as well. In order to reduce cogging torque and mitigate torque ripple to achieve sinusoidal output voltage and current profile, this paper utilizes various techniques i.e., chamfering, notching, eccentric circular shape and sine shape rotor techniques (as shown in Figure. 27) which is thoroughly discussed in author previous studies [52]. Variation of the inner/outer rotor cogging torque profile, inner/outer rotor instantaneous torque, and load profile (output voltage and current) is shown in Figure. 28, 29 and 30, respectively whereas quantitative values are listed in table 3. From Figure. 28, it can be clearly seen that rotor pole shaping effectively suppressed cogging torque in both inner and outer rotor. Detail quantitative analysis from the table 3 reveals that in comparison with the initial original rotor pole shape, inner rotor shape with chamfering, notching, eccentric circle, and sine shape reduces cogging torque by 31.56%, 50.45%, 65.2% and 66.62%, respectively whereas for outer rotor cogging torque is mitigated by 44.42%, 50.65%, 66.56% and 67.33%, respectively.

Since, cogging torque is suppressed which result reduced pulsation of the instantaneous torque as shown Figure. 29 ensuing reduced torque ripples in both outer and inner rotor. Analysis unveils that in case of inner rotor with chamfering, notching, eccentric circle and sine shape rotor, torque ripple is truncated by 50.35%, 54.13%, 55.81%, and 58.43%, respectively whereas for outer rotor, torque ripples is reduced by 54.92%, 46.18%, 47.48%, and 62.92%, respectively.

In additional, it is noteworthy that rotor pole shaping results dominant effects of cogging torque and torque ripples reduction however, average torque is affected in case of chamfering and notching which results lower average torque whereas eccentric circle and sine shape slightly improves average torque at both inner and outer rotor. Moreover, due to ripples content reduction and elimination of the higher order harmonics content, the output profile of the voltage and current becomes more sinusoidal as shown in Figure. 30 that fitted best for grid connection and required for AC applications. Based on comparative analysis of different rotor pole shapes, it is evident that for the proposed DRCR-PMFSG design, reduced cogging torque, torque ripples due to reduction of 5th and 7th order dominant harmonics content as a result sinusoidal output voltage and current is achieved with sine shaped rotor without influencing average torque profile. It is worth mentioning that due to reduction of higher order harmonics content, total harmonic distortion of the load profile (voltage and current) is reduced from 8.75% to 3.89%. Comprehensive quantitative analysis of the torque profile of initial original design with rotor pole shaping reveals that maximum cogging torque is reduced by 67.33% and torque ripples are suppressed by 62.92% in case of outer rotor whereas for inner rotor, cogging torque and torque ripples are suppressed by 66.62% and 58.43%, respectively.

Finally, detailed comparative study of conventional DSCR-PMFSG, IR-PMFSG and OR-PMFSG cogging torque (as listed in table 2) with proposed DRCR-PMFSG design reveals that in case of inner rotor, DRCR-PMFSG with sine shaped rotor offer 84.4% reduced cogging torque than DSCR-PMFSG, 72.17% less cogging torque than IR-PMFSG and 79.52% reduced cogging torque than OR-PMFSG whereas in case of outer rotor, proposed DRCR-PMFSG exhibits 74.48%, 54.26%, and 66.35% less cogging torque than conventional DSCR-PMFSG, IR-PMFSG and OR-PMFSG, respectively.

TABLE 3. Torque profile of proposed DRCR-PMFSG with rotor pole shaping.

Torque profile (Nm)	Original	Chamfering	Notching	Eccentric circle	**Sine shape**
T_{a-in}	18.36	16.78	17.35	18.89	**18.51**
T_{a-out}	23.97	24.55	23.51	22.98	**24.09**
T_{c-in}	7.73	5.29	3.83	2.69	**2.58**
T_{c-out}	13.01	7.23	6.42	4.35	**4.24**
T_{r-in}	24.35	12.09	11.17	10.76	**10.12**
T_{r-out}	32.39	14.60	17.43	17.01	**12.01**

T_{a-in}= average torque of inner rotor, T_{a-out}= average torque of outer rotor, T_{c-in}= cogging torque of inner rotor, T_{c-out}= Cogging torque of outer rotor, T_{r-in}= torque ripple of inner rotor, T_{r-out}= torque ripple of outer rotor

VIII. CONCLUSION

In this paper, a novel DRCR-PMFSG for wind turbine applications is proposed and comparatively analyzed with conventional DSCR-PMFSG under static characteristics,

overload, and wide speed range for generating output power, voltage, current, power density, and efficiency. Compared with DSCR-PMFSG, the proposed DRCR-PMFSG demonstrates advantages of eliminating the requirements of slip rings and retain brushless operation. Moreover, quantitative comparative analysis under static Analysis evident that proposed DRCR-PMFSG exhibits 33.29% higher flux, suppressed cogging torque and torque ripples up to 53.48% and 67.45%, respectively. Furthermore, analysis under overload and over-speed exposes that in comparison with DSCRP-PMFSG, the proposed DRCR-PMFSG improves voltage regulation factor by 55.88%, output current enhanced by 67.9%, raise output voltage to 2.01 times and power density to 1.72 times while maintaining the efficiency of 90.195% and achieving stable voltage profile with load variation. However, in comparison with the inner and outer rotor topologies, the proposed DRCR-PMFSG shows disadvantages of complex structure. Finally, to justify effectiveness of proposed DRCR-PMFSG, a detailed comparative analysis with conventional designs is performed and to validates finite element analysis (FEA) utilizing JMAG Designer v.20.1 a comprehensive mathematical modelling based on sub-domain model is developed accounting stator slot and rotor pole combinations, magnetic saturation, and winding configuration.

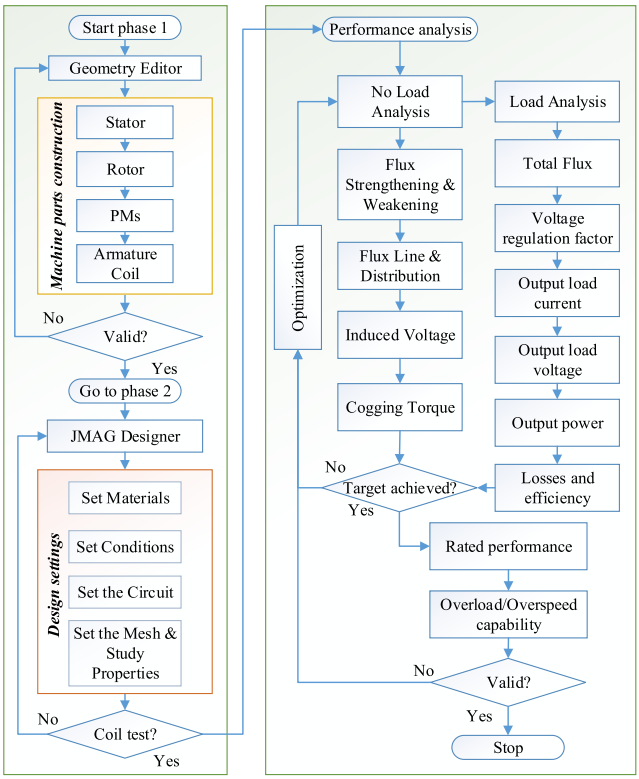

FIGURE 31. FEA based design process.

APPENDIX A: FEA BASED DESIGN PROCESS

FEA based design process is performed in two phases utilizing JMAG designer v20.1. Phase 1 is performed in geometry editor of JMAG whereas phase 2 is performed in JMAG designer. A detailed flow chart of the two phases is shown in Figure. 31.

It can be clearly seen that in phase 1 in geometry editor, different machine parts are designed based on design specification as listed in table 1. Once all design parameters are developed the model is imported to JMAG designer for phase 2. This phase consists of two parts. In first machine settings are done on the developed machine parts i.e., material is assigned to each part and conditioned are applied accordingly in such a way that rotation is applied to the rotors, circuit is developed for coil connections of armature windings and PM are assigned magnetization patter. Once all the pre-requisite conditional settings are done, mesh are developed, and coil test is performed.

In coil test, coil connection of armature windings is tested for no-load three phase flux linkage and sinusoidal three phase back-EMF. The coil connection obtained for the proposed DRCR-PMFSG is shown in Figure.1. Once, no-load test is performed and the required three phase flux and sinusoidal back-EMF is obtained, the model is shifted to performance analysis. In this case, first no-load performance is investigated and then on-load which are compared with conventional base reference and if the target doesn't meet then the model is procced for optimization for improving performance whereas if the required outputs are obtained, finally the model is procced for detailed analysis to test the model for rated performance and overload/overspeed capability.

REFERENCES

[1] *W. W. E. Association*. Accessed: Nov. 9, 2021. [Online]. Available: https://wwindea.org/information-2/statistics-news/

[2] M. D. Lellis, R. Reginatto, R. Saraiva, and A. Trofino, "The betz limit applied to airborne wind energy," *Renew. Energy*, vol. 127, pp. 32–40, Nov. 2018.

[3] W. Zhao, T. A. Lipo, and B. I. Kwon, "A novel dual-rotor, axial field, fault-tolerant flux-switching permanent magnet machine with high-torque performance," *IEEE Trans. Magn.*, vol. 51, no. 11, pp. 1–4, Nov. 2015.

[4] A. A. Pourmoosa and M. Mirsalim, "A transverse flux generator with a single row of permanent magnets: Analytical design and performance evaluation," *IEEE Trans. Ind. Electron.*, vol. 66, no. 1, pp. 152–161, Jan. 2019.

[5] W. Ullah, F. Khan, and E. Sulaiman, "Sub-domain modelling and multivariable optimisation of partitioned PM consequent pole flux switching machines," *IET Electr. Power Appl.*, vol. 14, no. 8, pp. 1360–1369, Aug. 2020.

[6] W. K. Ullah, S. Faisal, U. Erwan, U. Muhammad, and K. Noman, "Analytical validation of novel consequent pole E-core stator permanent magnet flux switching machine," *IET Electr. Power Appl.*, vol. 14, no. 5, pp. 789–796, 2020.

[7] W. Ullah, F. Khan, M. Umair, and B. Khan, "Analytical methodologies for design of segmented permanent magnet consequent pole flux switching machine: A comparative analysis," *COMPEL Int. J. Comput. Math. Electr. Electron. Eng.*, vol. 40, no. 3, pp. 744–767, Aug. 2021.

[8] W. Ullah, F. Khan, E. Sulaiman, I. Sami, and J.-S. Ro, "Analytical subdomain model for magnetic field computation in segmented permanent magnet switched flux consequent pole machine," *IEEE Access*, vol. 9, pp. 3774–3783, 2021.

[9] Z. Q. Zhu, Y. Pang, D. Howe, S. Iwasaki, R. Deodhar, and A. Pride, "Analysis of electromagnetic performance of flux-switching permanent-magnet machines by nonlinear adaptive lumped parameter magnetic circuit model," *IEEE Trans. Magn.*, vol. 41, no. 11, pp. 4277–4287, Nov. 2005.

[10] Y. Tang, E. Motoasca, J. J. H. Paulides, and E. A. Lomonova, "Comparison of flux-switching machines and permanent magnet synchronous machines in an in-wheel traction application," *COMPEL Int. J. Comput. Math. Electr. Electron. Eng.*, vol. 32, no. 1, pp. 153–165, Dec. 2012.

[11] X. Zhu, Z. Shu, L. Quan, Z. Xiang, and X. Pan, "Design and multicondition comparison of two outer-rotor flux-switching permanent-magnet motors for in-wheel traction applications," *IEEE Trans. Ind. Electron.*, vol. 64, no. 8, pp. 6137–6148, Aug. 2017.
[12] W. Hua, H. L. Zhang, M. Cheng, J. Meng, and C. Hou, "An outer-rotor flux-switching permanent-magnet-machine with wedge-shaped magnets for in-wheel light traction," *IEEE Trans. Ind. Electron.*, vol. 64, no. 1, pp. 69–80, Jan. 2017.
[13] X. Li, S. Liu, and Y. Wang, "Design and analysis of a new HTS dual-rotor flux-switching machine," *IEEE Trans. Appl. Supercond.*, vol. 27, no. 4, pp. 1–5, Jun. 2017.
[14] J.-W. Kwon and B.-I. Kwon, "Design of novel high performance dual rotor flux-switching drum winding machine," *J. Electr. Eng. Technol.*, vol. 14, no. 5, pp. 2019–2025, Sep. 2019.
[15] J. Chen, C. V. Nayar, and L. Xu, "Design and finite-element analysis of an outer-rotor permanent-magnet generator for directly coupled wind turbines," *IEEE Trans. Magn.*, vol. 36, no. 5, pp. 3802–3809, Sep. 2000.
[16] C. Yu and S. Niu, "Development of a magnetless flux switching machine for rooftop wind power generation," *IEEE Trans. Energy Convers.*, vol. 30, no. 4, pp. 1703–1711, Dec. 2015.
[17] A. Selema, "Development of a three-phase dual-rotor magnetless flux switching generator for low power wind turbines," *IEEE Trans. Energy Convers.*, vol. 35, no. 2, pp. 828–836, Jun. 2020.
[18] Y. Liu, H. Yu, and Y. Wang, "Establishment of a new dual rotor flux switching motor magnetic circuit model and optimization of no-load back EMF," *IEEE Trans. Magn.*, vol. 55, no. 12, pp. 1–5, Nov. 2019.
[19] M. Jafarboland and M. M. Sargazi, "Introducing a novel FSPM motor with double rotor and toroidal windings," *IET Electr. Power Appl.*, vol. 14, no. 7, pp. 1221–1227, Jul. 2020.
[20] X. Zhu, D. Fan, L. Mo, Y. Chen, and L. Quan, "Multiobjective optimization design of a double-rotor flux-switching permanent magnet machine considering multimode operation," *IEEE Trans. Ind. Electron.*, vol. 66, no. 1, pp. 641–653, Jan. 2019.
[21] A. Gandhi and L. Parsa, "Double-rotor flux-switching permanent magnet machine with yokeless stator," *IEEE Trans. Energy Convers.*, vol. 31, no. 4, pp. 1267–1277, Dec. 2016.
[22] Z. Xiang, L. Quan, X. Zhu, J. Huang, and D. Fan, "Investigation of optimal split ratio in brushless dual-rotor flux-switching permanent magnet machine considering power allocation," *IEEE Trans. Magn.*, vol. 54, no. 3, pp. 1–4, Mar. 2018.
[23] H. Hua and Z. Q. Zhu, "Novel partitioned stator hybrid excited switched flux machines," *IEEE Trans. Energy Convers.*, vol. 32, no. 2, pp. 495–504, Jun. 2017.
[24] Z. Q. Zhu, H. Hua, D. Wu, J. T. Shi, and Z. Z. Wu, "Comparative study of partitioned stator machines with different PM excitation stators," *IEEE Trans. Ind. Appl.*, vol. 52, no. 1, pp. 199–208, Jan./Feb. 2016.
[25] H. Hua, Z. Q. Zhu, C. Wang, M. Zheng, Z. Wu, D. Wu, and X. Ge, "Partitioned stator machines with NdFeB and ferrite magnets," *IEEE Trans. Ind. Appl.*, vol. 53, no. 3, pp. 1870–1882, May/Jun. 2017.
[26] C. C. Awah, Z. Q. Zhu, Z. Z. Wu, H. L. Zhan, J. T. Shi, D. Wu, and X. Ge, "Comparison of partitioned stator switched flux permanent magnet machines having single- or double-layer windings," *IEEE Trans. Magn.*, vol. 52, no. 1, pp. 1–10, Jan. 2016.
[27] D. J. Evans and Z. Q. Zhu, "Novel partitioned stator switched flux permanent magnet machines," *IEEE Trans. Magn.*, vol. 51, no. 1, pp. 1–14, Jan. 2015.
[28] C. H. T. Lee, J. L. Kirtley, and M. Angle, "A partitioned-stator flux-switching permanent-magnet machine with mechanical flux adjusters for hybrid electric vehicles," *IEEE Trans. Magn.*, vol. 53, no. 11, pp. 1–7, Nov. 2017.
[29] A. Zulu, B. C. Mecrow, and M. Armstrong, "Permanent-magnet flux-switching synchronous motor employing a segmental rotor," *IEEE Trans. Ind. Appl.*, vol. 48, no. 6, pp. 2259–2267, Nov./Dec. 2012.
[30] T. Guo, N. Schofield, and A. Emadi, "Double segmented rotor switched reluctance machine with shared stator back-iron for magnetic flux passage," *IEEE Trans. Energy Convers.*, vol. 31, no. 4, pp. 1278–1286, Dec. 2016.
[31] W. Ding, S. Yang, Y. Hu, S. Li, T. Wang, and Z. Yin, "Design consideration and evaluation of a 12/8 high-torque modular-stator hybrid excitation switched reluctance machine for EV applications," *IEEE Trans. Ind. Appl.*, vol. 64, no. 12, pp. 9221–9232, Dec. 2017.
[32] Y. Li, D. Bobba, and B. Sarlioglu, "Design and performance characterization of a novel low-pole dual-stator flux-switching permanent magnet machine for traction application," *IEEE Trans. Ind. Appl.*, vol. 52, no. 5, pp. 4304–4314, Sep./Oct. 2016.
[33] M. Liu, Y. Li, W. Sixel, and B. Sarlioglu, "Design and testing of low pole dual-stator flux-switching permanent magnet machine for electric vehicle applications," *IEEE Trans. Veh. Technol.*, vol. 69, no. 2, pp. 1464–1472, Feb. 2020.
[34] Y. Gao, D. Li, R. Qu, and H. Ding, "A double-stator flux switching PM machine with multi-PM MMF harmonics," *IEEE Trans. Magn.*, vol. 55, no. 6, pp. 1–6, Jun. 2019.
[35] W. Yu, K. Liu, W. Hua, M. Hu, Z. Zhang, and J. Hu, "A new high-speed dual-stator flux switching permanent magnet machine with distributed winding," *IEEE Trans. Magn.*, early access, May 25, 2021, doi: 10.1109/TMAG.2021.3082931.
[36] Y. Jiang, J. Zhang, and T. Li, "A segmented brushless doubly fed generator for wind power applications," *IEEE Trans. Mag.*, vol. 54, no. 3, pp. 1–4, Mar. 2018.
[37] R. Nasiri-Zarandi, A. Ghaheri, and K. Abbaszadeh, "Thermal modeling and analysis of a novel transverse flux HAPM generator for small-scale wind turbine application," *IEEE Trans. Energy Convers.*, vol. 35, no. 1, pp. 445–453, Mar. 2020.
[38] S. A. Mirnikjoo, K. Abbaszadeh, and S. E. Abdollahi, "Multiobjective design optimization of a double-sided flux switching permanent magnet generator for counter-rotating wind turbine applications," *IEEE Trans. Ind. Electron.*, vol. 68, no. 8, pp. 6640–6649, Aug. 2021.
[39] S. Mirnikjoo, F. Asadi, K. Abbasazdeh, and S. E. Abdollahi, "Effect of rotor topology on the performance of counter-rotating double-sided flux switching permanent magnet generator," *IEEE Trans. Energy Convers.*, early access, Aug. 10, 2021, doi: 10.1109/TEC.2021.3103555.
[40] J. T. Chen and Z. Q. Zhu, "Winding configurations and optimal stator and rotor pole combination of flux-switching PM brushless ac machines," *IEEE Trans. Energy Convers.*, vol. 25, no. 2, pp. 293–302, Jun. 2010.
[41] A. A. Arkadan, T. M. Hijazi, and B. Masri, "Design evaluation of conventional and toothless stator wind power axial-flux PM generator," *IEEE Trans. Magn.*, vol. 53, no. 6, pp. 1–4, Jun. 2017.
[42] W. Hua, M. Cheng, Z. Q. Zhu, and D. Howe, "Analysis and optimization of back EMF waveform of a flux-switching permanent magnet motor," *IEEE Trans. Energy Convers.*, vol. 23, no. 3, pp. 727–733, Jul. 2008.
[43] K. Boughrara, R. Ibtiouen, D. Žarko, O. Touhami, and A. Rezzoug, "Magnetic field analysis of external rotor permanent-magnet synchronous motors using conformal mapping," *IEEE Trans. Magn.*, vol. 46, no. 9, pp. 3684–3693, Sep. 2010.
[44] N. Ullah, F. Khan, W. Ullah, A. Basit, M. Umair, and Z. Khattak, "Analytical modelling of open-circuit flux linkage, cogging torque and electromagnetic torque for design of switched flux permanent magnet machine," *J. Magn.*, vol. 23, no. 2, pp. 253–266, Jun. 2018.
[45] W. Ullah, F. Khan, and M. Umair, "Lumped parameter magnetic equivalent circuit model for design of segmented PM consequent pole flux switching machine," *Eng. Comput.*, vol. 38, no. 2, pp. 572–585, Feb. 2021.
[46] W. Ullah, F. Khan, E. Sulaiman, M. Umair, and N. Ullah, "2-D analytical modelling of novel consequent pole linear permanent magnet flux switching machine," *J. Brazilian Soc. Mech. Sci. Eng.*, vol. 43, no. 6, p. 307, Jun. 2021.
[47] L. Wu, H. Yin, D. Wang, and Y. Fang, "On-load field prediction in SPM machines by a subdomain and magnetic circuit hybrid model," *IEEE Trans. Ind. Electron.*, vol. 67, no. 9, pp. 7190–7201, Sep. 2020.
[48] L. Wu, H. Yin, D. Wang, and Y. Fang, "A nonlinear subdomain and magnetic circuit hybrid model for open-circuit field prediction in surface-mounted PM machines," *IEEE Trans. Energy Convers.*, vol. 34, no. 3, pp. 1485–1495, Sep. 2019.
[49] Y. Oner, Z. Q. Zhu, L. J. Wu, X. Ge, H. L. Zhan, and J. T. Chen, "Analytical on-load subdomain field model of permanent-magnet Vernier machines," *IEEE Trans. Ind. Electron.*, vol. 63, no. 7, pp. 4105–4117, Jul. 2016.
[50] K. Boughrara, T. Lubin, and R. Ibtiouen, "General subdomain model for predicting magnetic field in internal and external rotor multiphase flux-switching machines topologies," *IEEE Trans. Magn.*, vol. 49, no. 10, pp. 5310–5325, Oct. 2013.
[51] A. Jabbari, "Analytical modeling of magnetic field distribution in multiphase H-type stator core permanent magnet flux switching machines," *Iranian J. Sci. Technol., Trans. Electr. Eng.*, vol. 43, no. S1, pp. 389–401, Jul. 2019.
[52] W. Ullah, F. Khan, E. Sulaiman, and M. Umair, "Torque characteristics of high torque density partitioned PM consequent pole flux switching machines with flux barriers," *CES Trans. Electr. Mach. Syst.*, vol. 4, no. 2, pp. 130–141, Jun. 2020.

[53] L. Shao, W. Hua, J. Soulard, Z.-Q. Zhu, Z. Wu, and M. Cheng, "Electromagnetic performance comparison between 12-phase switched flux and surface-mounted PM machines for direct-drive wind power generation," *IEEE Trans. Ind. Appl.*, vol. 56, no. 2, pp. 1408–1422, Mar. 2020.

[54] U. B. Akuru and M. J. Kamper, "Intriguing behavioral characteristics of rare-earth-free flux switching wind generators at small- and large-scale power levels," *IEEE Trans. Ind. Appl.*, vol. 54, no. 6, pp. 5772–5782, Nov. 2018.

[55] W. Ullah, F. Khan, and S. Hussain, "Investigation of inner/outer rotor permanent magnet flux switching generator for wind turbine applications," *IEEE Access*, vol. 9, pp. 149110–149117, 2021.

[56] U. B. Akuru and M. J. Kamper, "Formulation and multiobjective design optimization of wound-field flux switching machines for wind energy drives," *IEEE Trans. Ind. Electron.*, vol. 65, no. 2, pp. 1828–1836, Feb. 2018.

[57] W. Ullah and F. Khan, "Design and performance analysis of a novel outer-rotor consequent pole permanent magnet machine with H-type modular stator," *IEEE Access*, vol. 9, pp. 125331–125341, 2021.

WASIQ ULLAH (Graduate Student Member, IEEE) was born in Peshawar, Khyber Pakhtunkhwa, Pakistan, in 1995. He received the B.S. and M.S. degrees in electrical (power) engineering from COMSATS University Islamabad (Abbottabad Campus), Abbottabad, Pakistan, in 2018 and 2020, respectively, where he is currently pursuing the Ph.D. degree in electrical (power) engineering.

Since 2018, he has been a Research Associate with the Electric Machine Design Research Laboratory. His research interests include analytical modeling, design analysis and optimization of permanent magnet flux switching machines, linear flux switching machines, hybrid excited flux switching machines, novel consequent pole flux switching machines for high-speed brushless AC applications, and flux switching generators for counter-rotating wind turbines applications.

Mr. Ullah is basically from Afghanistan and serves as a Reviewer for IEEE Access, *IET Electric Power Application*, and 2022 IEEE Energy Conversion Congress and Exposition (ECCE 2022). He is a member of IEEE-IES Electrical Machines Technical Committee Members and a member of Pakistan Engineering Council.

FAISAL KHAN (Member, IEEE) was born in Charsadda, Khyber Pakhtunkhwa, Pakistan, in 1986. He received the B.S. degree in electronics engineering and the M.S. degree in electrical engineering from COMSATS University Islamabad (Abbottabad Campus), Pakistan, in 2009 and 2012, respectively, and the Ph.D. degree in electrical engineering from Universiti Tun Hussein Onn Malaysia, Malaysia, in 2017.

From 2010 to 2012, he was a Lecturer with the University of Engineering & Technology, Abbottabad, Pakistan. Since 2017, he has been an Assistant Professor with the Electrical and Computer Engineering Department, COMSATS University Islamabad (Abbottabad Campus). He is currently the Head of the Electric Machine Design Research Laboratory. He is the author of more than 100 publications, one patent, and received multiple research awards. His research interests include design and analysis of flux-switching machines, synchronous machines, and DC machines.

He is a member of IEEE-IES Electrical Machines Technical Committee.

SHAHID HUSSAIN (Graduate Student Member, IEEE) was born in Swabi, Khyber Pakhtunkhwa, Pakistan. He received the B.S. degree in electrical power engineering from COMSATS University Islamabad, Abbottabad Campus, Abbottabad, Pakistan, in 2019, where he is currently pursuing the M.S. degree in electrical power engineering. He has been a Research Assistant with the Electric Machine Design Research Laboratory, since 2020. His research interests include design analysis, optimization and experimental validation of modular and complementary fault tolerant field excited linear flux switching machines for long stroke application. He is a member of Pakistan Engineering Council.